12-2015

How Does the Connectivity of Open-Framework Conglomerates within Multi-Scale Hierarchical Fluvial Architecture Affect Oil-Sweep Efficiency in Waterflooding?

Naum I. Gershenzon
Wright State University - Main Campus, naum.gershenzon@wright.edu

Mohamad Reza Soltanian

Robert W. Ritzi
Wright State University - Main Campus, robert.ritzi@wright.edu

David F. Dominic
Wright State University - Main Campus, david.dominic@wright.edu

Don Keefer

See next page for additional authors

How does the connectivity of open-framework conglomerates within multi-scale hierarchical fluvial architecture affect oil sweep efficiency in waterflooding?

Naum I. Gershenzon[1], Mohamad Reza Soltanian[1], Robert W. Ritzi Jr. [1], David F. Dominic[1], Don Keefer[2], Eric Shaffer[2], Brynne Storsved[2]

[1] *Department of Earth and Environmental Sciences, Wright State University, 3640 Col. Glenn Hwy., Dayton, OH 45435*

[2]*Illinois State Geological Survey, University of Illinois, Urbana-Champaign*

ABSTRACT

Understanding multiphase fluid flow and transport processes within aquifers, candidate reservoirs for CO2 sequestration, and petroleum reservoirs requires understanding a diverse set of geologic properties of the aquifer or reservoir, over a wide range of spatial and temporal scales. We focus on multiphase flow dynamics with wetting (e.g. water) and non-wetting (e.g. gas or oil) fluids, with one invading another. This problem is of general interest in a number of fields, and is illustrated here in considering how the sweep efficiency of oil during a waterflood is affected by heterogeneity at multiple scales within geologic models. Using a relatively fine-resolution grid throughout a relatively large domain in these simulations, and probing the results with advanced scientific visualization tools (RVA/Paraview) promotes a better understanding of how smaller-scale features affect the aggregate behavior at larger scales. We studied the effects

on oil sweep efficiency of the proportion, hierarchical organization, and connectivity of high-permeability open-framework conglomerate (OFC) cross-sets within the multi-scale stratal architecture found in fluvial deposits. We analyzed oil production rate, water breakthrough time, and spatial and temporal distribution of residual oil saturation. As expected, the effective permeability of the reservoir exhibits large-scale anisotropy created by the organization of OFC cross-sets within unit bars, and the organization of unit bars within compound bars. As a result oil sweep efficiency critically depends on the direction of the pressure gradient. However, contrary to expectations, the total amount of trapped oil due to the effect of capillary trapping does not depend on the magnitude of the pressure gradient within the examined range. Hence the pressure difference between production and injection wells does not affect sweep efficiency, although the spatial distribution of oil remaining in the reservoir depends on this value. Whether or not clusters of connected OFC span the domain does not affect sweep efficiency, only the absolute rate of oil production.

INTRODUCTION

Multiphase fluid flow and transport processes within aquifers, candidate reservoirs for CO2 sequestration, and petroleum reservoirs are affected by geologic heterogeneity in ways that are not fully understood. In addition to advancing basic science, this area of research can contribute to solving societal problems such as remediating contaminated aquifers, reducing greenhouse gas emissions, and improving oil recovery. The uncertainty about site-specific geology stems from the inherent variation in reservoir properties, which in sedimentary reservoirs is controlled by the depositional environments in which they were formed. Understanding subsurface flow dynamics requires understanding a diverse set of geologic

properties of the aquifer or reservoir, over a wide range of spatial and temporal scales. Historically, aquifer and reservoir modeling has tended to aggregate parameters across scales because the direct representation of smaller scale features has not been computationally tractable. Advances in high-performance computing have now made it possible to represent reservoir properties over a broad range of spatial scales within one model. When small-scale features are represented, smaller scale processes can be studied directly and differentiated from their cumulative effect on reservoir-scale processes (e.g., Scheibe et al., 2015). In this context, recent studies have focused on the connectivity of sedimentary units having higher intrinsic permeability, which can form preferential flow pathways (e.g. Guin et al., 2010). New research has produced quantitative models for the spatial distribution of sedimentary units across a wide range of scales, especially for deposits created by fluvial processes (e.g. Lunt et al., 2014). This success has, in turn, led to new methods for creating digital geologic models representing this range of scales (e.g. Ramanathan et al., 2010).

This article involves a nexus of these areas of research. We focus on multiphase flow dynamics with wetting (e.g. water) and non-wetting (e.g. gas or oil) fluids, with one invading another. This problem is of general interest in a number of fields, and is illustrated here in considering how the sweep efficiency of oil during a waterflood is affected by heterogeneity at multiple scales within geologic models. Recent work on this problem has included new ideas on the sedimentology in fluvial channel-belt deposits across a range of spatial scales, new ways of creating digital geologic models that represent this multi-scaled sedimentary heterogeneity, new ideas for quantifying the connectivity of preferential flow pathways across this range of scales, and new efforts in using high-performance computing to simulate multiphase fluid flow dynamics (e.g. Gershenzon et al., 2015). Using a relatively fine-resolution grid throughout a

relatively large domain in these simulations promotes a better understanding of how smaller-scale features affect the aggregate behavior at larger scales. The results thus far have generated interesting insights, especially how these features affect the capillary trapping of oil, and thus the sweep efficiency of waterflooding. In some cases these results are counterintuitive. In this article, we continue to explore this problem by probing the results with advanced scientific visualization tools. These explorations confirm and more fully support previous results, and better clarify the underlying processes.

BACKGROUND

Oil sweep efficiency during waterflooding is fundamentally controlled by the nature of immiscible displacement of a non-wetting liquid by a wetting liquid in porous media (Buckley and Leverett, 1942). This process includes the effects of capillary pressure and relative permeability on oil trapping and early water breakthrough (Kortekaas, 1985; Corbett et al., 1992; Khataniar and Peters, 1992; Wu et al., 1993; Gharbi et al., 1997; Kaasschieter, 1999). Such immiscible displacement is, in turn, controlled by the three-dimensional heterogeneity and anisotropy in permeability (Kjonsvik et al., 1994; Jones et al., 1995; Tye et al., 2003; Choi et al., 2011). In sedimentary reservoirs, the three-dimensional heterogeneity and anisotropy is controlled by the architecture of the sedimentary deposits.

Recent studies have led to new conceptual and quantitative models for sedimentary architecture in fluvial deposits over a range of scales that are relevant to the performance of some important petroleum reservoirs (Tye et al., 2003; Lunt et al., 2004; Bridge, 2006; Lunt and Bridge 2007). As shown in Figure 1, braided channel-belt deposits are characterized by a large

volume fraction of convex-up, bar deposits formed within channels. Only when channels are abandoned and filled are "channel-shaped" units formed. Created during lower-energy flow conditions, these concave-up channel fills are low-permeability baffles within the channel belts. In gravelly channel-belt deposits, preferential flow pathways arise from the interconnection of open-framework gravels within lobate unit bar deposits (Lunt and Bridge, 2007). These are the "thief zones" within reservoirs that have a negative effect on oil recovery (McGuire et al., 1994; 1999; Tye et al., 2003).

Lunt et al. (2004 a,b) studied the gravelly channel belt of the Sagavanirktok River (Alaska, Fig. 1), a modern analog for deposition of the Ivishak Formation in Prudhoe Bay field, Alaska and quantified the proportions and lengths for sedimentary unit types, or facies, across relevant scales (Table 1). At the smallest scale, sets of cross-stratified ("cross-sets" herein) sand, sandy gravel, and open-framework gravel (decimeters thick and meters long) occur within unit bar deposits (tens of decimeters thick and tens of meters long). Unit bars and cross-bar channel fills occur within compound bar deposits (meters thick and hundreds of meters long). Compound bar deposits and the channel fills that bound them occur within channel belts (tens of meters thick and kilometers long). Importantly, the open-framework gravel cross-sets were found to make up 25 to 30 percent of the volume of the deposit. These sedimentary unit types are preserved with similar lengths and proportions within the Victor interval of the Ivishak Formation. (Tye et al., 2003). The Victor interval has few shales or other vertical permeability barriers, and connected cross-sets of open-framework conglomerates (i.e., lithified open-framework gravels, referred to as OFC hereafter) are the dominant control on reservoir performance (McGuire et al., 1994, 1999; Tye et al., 2003).

The sedimentary architecture quantified by Lunt et al. (2004 a,b) was incorporated by Ramanathan et al. (2010) into a high-resolution, three-dimensional, digital model using geometric-based simulation methods. This model was used to investigate how the spatial variations in reservoir properties (relative permeability and capillary pressure) affect oil sweep efficiency in waterflooding (Gershenzon et al., 2015).

Some of the results revealed nuances that compliment to conventional understanding. For example, it is known that anisotropy affects sweep efficiency, and that a pair of injector and producer wells should be aligned perpendicular to the principle direction of anisotropy to maximize efficiency (Rose et al., 1989). The hierarchical stratal architecture in Figure 1 includes preferential-flow pathways through higher-permeability OFC units, which differ with scale and direction. The net influence creates anisotropy in the bulk effective permeability, and indeed sweep efficiency in these simulations was found to be greater with the injector/producer pair is aligned normal the paleoflow direction (i.e., the orientation of the channel belt) as compared to alignment parallel to paleoflow direction (Gershenzon et al., 2015), as expected. However, some of the related results are counter to conventional understanding and need to be further explored.

One such result relates to how efficiency varies with pressure gradient. During immiscible oil displacement, oil is trapped due to reservoir heterogeneities in both permeability and capillary pressure (Kortekaas, 1985; Wu et al., 1993; Kaasschieter, 1999). It has been previously shown that the trapping effect, and hence oil sweep efficiency, depends on the pressure gradient (Corbett et al., 1992). However, in the high-resolution simulations of a fluvial reservoir, Gershenzon et al. (2015) found that the value of the pressure gradient has little effect on oil sweep efficiency but does influence the spatial distribution of oil remaining in the reservoir depends on this value. These results indicate that the amount of oil trapped in isolated

OFC strata sets is offset by the amount of oil moving out of surrounding sandstone and through connected OFC cross-sets.

Another surprising result relates to the effect of heterogeneity on fingering of the waterfront. Because the contrast in permeability between OFC and sandstone is large and because the size of OFC connected pathways considerably exceeds the cell size in the model, it was expected that the waterfront would show large-scale fingering. However, fingering was not observed in any of the reservoir realizations (Gershenzon et al., 2015). Even so, most of the oil (80-95%) reached the production well through connected OFC pathways.

Finally, it was surprising that oil sweep efficiency did not strongly depend on the proportion of open-framework conglomerate in the reservoir. The existence of OFC pathways depend upon proportion. When the proportion of OFC is above 20% of the deposit by volume there are connected pathways through OFC which span the reservoir in any direction ("percolate" in the field of percolation theory), and when the proportion is below 20% the pathways do not span (Guin and Ritzi, 2008; Guin et al., 2010). Simulations were performed in which the proportion of OFC was systematically varied across this threshold percentage, and the presence/absence of spanning pathways was confirmed. However, the presence/absence of connected pathways through OFC did not abruptly affect oil sweep efficiency (Gershenzon et al., 2015).

The above-mentioned specific behaviors of waterflooding processes are not intuitive and need to be further explored. The goal of this article is to further investigate these behaviors and to provide a more complete description of the observed processes**.** The Reservoir Visualization Analysis (RVA) software (Keefer et al., 2012) built on the ParaView open-source platform (http://rva.cs.illinois.edu/index.html) was used to further visualize, analyze, and illustrate our

results. We first provide a description of the reservoir model and the methodology for reservoir simulation and analysis, followed by results, discussion and conclusions.

METHODOLOGY

Geocellular Model for Reservoir Architecture

New approaches have been developed for creating digital models that reproduce the multi-scaled and hierarchical architecture in fluvial channel-belt deposits (e.g. Ramanathan et al., 2010; Hassanpour et al., 2013). This approach preserves architectural information within any gridding scheme used to create geocellular (i.e. discretized) models intended for flow and transport simulation. We adapted the method of Ramanathan et al. (2010) to create a geocelluar model for the hierarchy of unit types in Table 1, for the purposes of computational experiments for studying the waterflood of an Ivishak-type reservoir, i.e. a reservoir exhibiting heterogeneity as described by Lunt et al. (2004 a,b) and as illustrated in Figure 1. In this method, a hierarchical geometric-based model of the multi-scaled facies architecture is first created, which is defined continuously over space. At each hierarchical level, stratal units are created using piecewise planar polyhedral elements. These are then combined into a global coordinate system with typically only pieces of them preserved, according to rules based on depositional processes. For example, Figs. 2a-b show how unit bar deposits are created as an assemblage within a compound bar deposits. In the same general way, cross-sets are created in assemblages populating unit bar deposits (Fig. 3). In a second step, the geometric model is sampled on a grid to create a geocellular model of the geologic architecture (Figs 2c-d). The digital model can be created (and recreated) from the geometric model for all or part of the global domain, with any desired grid

183 resolution that suits the flow modelers. Petrophysical properties are mapped into the geocellular
184 model from statistical distribitions defined per strata type I textural facies type, and thus with a
185 resolution smaller than the smallest facies.

186 Guin et al. (2010) confirmed that the approach creates a hierarchy of sedimentary unit
187 types that honor the proportions, geometries, and spatial distribution of the unit types quantified
188 in natural deposits at each level by Lunt et al. (2004 a,b). Figure 3 shows a cross section through
189 an extracted piece of a simulated compound bar deposit sampled with fine resolution (additional
190 simulations showing larger-scale architecture are given in Ramanathan et al. (2010), Fig. 10).

191 The cross-sets of high-permeability open-framework conglomerate (OFC) are simulated
192 discretely. OFC cells are considered to be connected in a cluster when cell faces are adjacent.
193 Importantly, clusters of continuously connected OFC cells create preferential flow pathways.
194 When OFC cross-sets comprise at least 20% of the volume of the deposit, clusters span opposing
195 pairs of domain boundaries (Guin et al., 2010). Such spanning, preferential-flow pathways have
196 been inferred to exist within the Ivishak Formation (Tye et al., 2003). The number, size, and
197 orientation of OFC clusters in the geocellular model change with proportion. At any given
198 proportion, the number, size, and orientation of clusters changes across the different hierarchical
199 levels (scales) of the stratal architecture. Connected OFC cells within individual cross-sets form
200 paths that vertically span single unit bar deposits. Connections across unit bar boundaries
201 enhance lateral branching and the many clusters within unit bars connect into a smaller number
202 of larger clusters at the scale of multiple unit bars. At the scale of a whole compound bar deposit,
203 these clusters are typically connected into one or two large, spanning clusters. The spanning
204 clusters occur at proportions of open-framework gravel cells below the theoretical threshold
205 (31%) for random infinite media predicted in the mathematical theory of percolation. Guin and

Ritzi (2008) showed that this is caused by geological structure within a finite domain. The percolation theory shows why two-dimensional models under-represent true three-dimensional connectivity, and thus why simulations must be three-dimensional (Huang et al., 2012).

Multiphase Flow Simulations

We simulated 3D immiscible oil displacement by water (black oil approximation) with ECLIPSE (Schlumberger Reservoir simulation software, version 2010.2). The highly non-linear nature of the flow equations creates a significant challenge to obtaining computationally convergent solutions, and currently limits us to simulations of a modest reservoir size. Our goal is to eventually grow the problem to larger domains with finer resolution. The top of the parallelepiped reservoir model is taken to be at a depth of 2560 m (8400 feet). The size of the reservoir in the *x*, *y* and *z* directions are L_x=200 m (656 feet), L_y=200 m (656 feet) and L_z=5 m (16.4 feet), respectively. This encompasses the heterogeneity created by an assemblage of unit bars within a compound bar. The reservoir is divided into one million cells with cell size 2:2:0.05 m in the *x*, *y* and *z* directions, respectively.

We generated six realizations of the reservoir volume, each with a different proportion of OFC (Table 2) using the method (Ramanthan et al., 2010) described above. As shown in Table 2, the proportion of OFC affects the proportion of high-permeability cells that are connected to create preferential flow pathways. We consider clusters to span opposing boundaries when their extent in *x*, *y* and *z* directions is equal to the domain size in those directions. Thus, the reservoir models range from one with more than 90% of all OFC cells connected in one spanning cluster (realization 1) to those with no spanning cluster (realizations 5 and 6). Figure 4 shows realizations 1, 4 and 6 with 28%, 22% and 16% of OFC cells, respectively. The blue color

indicates the OFC cells. Although it is not obvious from Figure 4, realization 1 (bottom panel) incorporates almost all OFC cells (90%) in one spanning cluster, realization 4 (middle panel) has one spanning cluster (55% of all OFC cells) and realization 6 (top) has no spanning clusters. The RVA/Paraview visualization package facilitated filtering out connected clusters and rendering images of them. Figure 5 displays the same realizations but only OFC cells are shown. Figure 5 illustrates that OFC cells are densely interconnected in all considered cases, although the distributions of OFC material between spanning and non-spanning clusters are very different among these realizations. As we will demonstrate later, the existence of this "small-scale dense net" explains the main features of waterflooding in fluvial reservoirs. Figure 6 shows the five largest clusters of realization 4; the largest cluster is a spanning cluster.

The saturated permeability in sandy-gravel deposits (and of their lithified equivalents, pebbly sandstones and sandy conglomerates) varies non-linearly as a function of the volume of sand mixed with gravel (see Fig. 6 in Ramanathan et al., 2010; see also Klingbeil et al., 1999; Conrad et al., 2008). Sandy-gravel strata have permeabilities similar to the sand they contain, which are of the order of 10^0 to 10^1 Darcies. Thus, sand and sandy-gravel cross-sets within unit bars have permeabilities similar to channel-fill sands. Open-framework gravels have permeabilities of the order of 10^3 to 10^4 Darcies. In either type of strata, the coefficient of variation in permeability is of the order of unity. In the lithified stratatypes within the Ivishak Formation (sandstones, pebbly sandstones and open-framework conglomerates), the saturated permeabilities scale down accordingly, and following Tye et al. (2003) the geometric mean for saturated permeability of sandstones and pebbly sandstones is taken to be 66 milli-Darcies (mD) in this study. Because these two lithotypes are assigned the same permeability distribution in the simulations, we refer to them collectively as "sandstone." Furthermore, the geometric mean

saturated permeability of OFC is taken to be 5250 mD. Within all these lithotypes, lognormal permeability distributions were used, as is found in natural deposits (e.g. Conrad et al., 2008). The permeability from each distribution is randomly mapped into each cross-set from the appropriate distribution (i.e. the model does not represent spatial correlation below the scale of a cross-set). Figure 7 shows the distributions of lithotypes and permeability for two realizations. Figure 8 shows the permeability distributions for realizations 1 and 6. The percentage of cells with permeability in each specified range is also shown. While the percentage of material with high permeability is different between these two cases, the common features are: (1) The majority of cells have permeability less than 1 D. (2) The second maximum in permeability distribution is in the range from 3 to 4 D. The latter range brackets the geometric average of permeability of all OFC cells. (3) The cells with permeability inside of each range connect to small-scale (compared with reservoir size) networks in all ten considered ranges of permeability. We did not include cell-scale anisotropy in the simulations, i.e. the ratio between vertical and horizontal permeability is unity, so that the effective anisotropy imparted by the simulated fluvial architecture, alone, could be observed.

Initially the reservoir contains oil with dissolved gas and connate water in equilibrium. Two different property characteristic curves were utilized for the sandstone and OFC lithotypes. These curves define the relations between water relative permeability, oil-in-water relative permeability, water-oil capillary pressure, gas relative permeability, and water saturation. Figure 9 shows the relative permeability and capillary pressure as a function of water saturation for sandstone and OFC lithotypes (see also Gershenzon et al., 2015 for more details).

Porosity of both lithotypes is 0.2. Irreducible water saturation is 0.256 for sandstone and 0.1 for OFC. Residual oil saturation is 0.3. At the reference pressure of 4014.7 psi (hydrostatic

pressure at a depth of 2560 m), the water formation volume factor is 1.029 rb/stb = rm^3/sm^3, the water viscosity is 0.31 cP, and the water and rock compressibility are 3.13×10^{-6} and 3.0×10^{-6} 1/psi, respectively. The oil, water and gas gravities at surface conditions are 23.5, 1.04 and 0.8, respectively.

Two different placements had been used for injection and production wells: (1) parallel to the direction of paleoflow utilized in constructing the reservoir realizations, which is in the (y) direction (coordinates of the injection well are x = 100 m, y = 20 m; coordinates of the production well are x = 100 m, y = 180 m) (see Fig. 12); (2) perpendicular to paleoflow in the (x) direction (coordinates of injection well are x = 20 m, y = 100 m; coordinates of production well are x = 180 m, y = 100 m). In the simulations the bottom hole pressure has been specified for both wells. We utilized values for the pressure difference between injection and production wells from 100 to 800 psi.

RESULTS AND DISCUSSION

Under conditions described above the water injection rate and the oil and water production rate ranges from 160 stb/day or 23% OOIP/year (reservoir realization #6, pressure difference 100 psi, wells placed perpendicular to paleoflow direction) to 3000 stb/day or 435% OOIP/year (reservoir realization #1, pressure difference 800 psi, wells placed along paleoflow direction). Figure 11 illustrates the oil and water production rates as function of time and show that the production rates change in time while the pressure difference between wells is constant. Figure 12 shows oil and water production rates as function of injected water volume for the six

297 modelled realizations (Table 1)) at a single pressure difference (i.e., 200 psi) between the
298 injector and producer wells.
299
300 Study of Anisotropy
301 The fluvial architecture represented in our model creates anisotropy in which the bulk
302 effective permeability in the paleoflow direction (*y*) differs from the effective permeability in the
303 direction normal to the paleoflow (*x*) (Guin et al., 2010). Also, the effective permeability in the
304 horizontal directions is very different from that in the vertical direction (*z*) (see Table 2). As
305 stated above, we did not include cell-scale anisotropy in the simulations so that this effective
306 anisotropy imparted by the simulated fluvial architecture, alone, could be observed. To consider
307 how the anisotropy affects the process of oil displacement, we compared results of simulations
308 with the pressure gradient along the *y* direction to the same case with the pressure gradient along
309 the *x* direction. Gershenzon et al. (2015) showed that the results are essentially the same for
310 gradients in the positive and the negative coordinate directions in each case. Therefore, the
311 orientation of the OFC strata is not a factor, and we only show results for the positive directions.
312 Figure 10 clearly illustrates the effects of anisotropy. Under the same pressure gradient between
313 injection and production wells, the waterflood front propagates faster when the pressure gradient
314 is in the *y* direction. The front is broader when the pressure gradient is in the *x* direction, so that a
315 larger volume of the reservoir is swept (see animation in Fig. 13). This qualitative result
316 illustrates why sweep efficiency increases if the injector and producer are aligned normal to the
317 paleoflow direction (see Table 3), and supports the values for sweep efficiency reported in
318 Gershenzon et al. (2015; see their Figs. 7-10).

Anisotropy can also be understood in terms of the sizes of the sandstone and OFC clusters in *x*, *y* and *z* directions (see Table 2). The mean size of both sandstone and OFC clusters in the paleoflow direction is almost double the size of the clusters normal to paleoflow horizontal direction for all realizations. Figures 6 and 14 clearly illustrate that most of the clusters are elongated the in paleoflow direction. Anisotropy is caused by the way OFC cross-sets are organized within the stratal architecture at larger scales.

Anisotropy in the vertical direction is even more dramatic. The difference in cluster size between horizontal and vertical directions ranges from 20 (x-direction) to 40 (y-direction) times (see Table 2).

Study of Lack of Fingering in the Waterfront

The existence and connectivity of high-permeability material in a fluvial reservoir influences waterflooding processes. Indeed, between 80% and 95% of oil comes to a production well through the OFC cells even though the total proportion of OFC cells is from 16% to 28%. This is not a surprise because the mean permeability of OFC is 80 times larger than sandstone. This difference in permeability might be expected to produce: (1) highly developed fingering of the water-oil front and (2) a pronounced difference in dynamics between reservoir realizations which include spanning OFC clusters and those without such clusters. However, Gershenzon et al. (2015; their figs. 9 and 11) showed that the oil production dynamics are not noticeably different between realizations with spanning OFC clusters (realizations 1-4) and those without spanning clusters (realizations 5 and 6) (see also Fig. 12). Moreover, the large-scale fingering of the water-oil front was not observed in any of the realizations. Indeed, as Figure 15 shows, the water-oil front is similar in each realization and has a relatively smooth shape, regardless of the

value of the pressure gradient. These features can be explained by the specific structure of the fluvial-type reservoir as follows. Note that in all reservoir realizations (1) small distances separate OFC clusters (and different branches of the same cluster) in the vertical direction (from 35 cm to 55 cm, see Table 2, column 7); and (2) the branches of OFC clusters are thin in the vertical direction (~10–15 cm). Figure 16 illustrates the typical pattern of oil flow between such structures. Oil moves preferably along the pressure gradient in high-permeability OFC clusters and diffuses preferably in the direction normal to OFC branches in the low-permeability sandstone. Because the distances between OFC branches are small and because capillary pressure pushes oil from the sandstone to the OFC, oil from sandstone cells reaches the OFC cells relatively quickly (the pressure difference between injection and production wells ranged from 100 to 800 psi). This process and the small thickness of the OFC branches explain both the absence of the large-scale fingering and the fact that most of the oil reaches the production well through the OFC clusters. As can be shown, even realizations with a small proportion of OFC material include large-scale clusters (although there are no spanning clusters). The same scenario of oil movement (Fig. 16) works also for those realizations, which explains the almost identical behavior (from sweep efficiency point of view) of waterfloding in all reservoir realizations.

Study of Oil Trapping as a Function of the Pressure Gradient and the Proportion of OFC

The dynamics of immiscible oil displacement by water is described by the Buckley-Leverett equation (Buckley and Leverett, 1942). Solutions of this equation for homogeneous media and neglecting capillary pressure indicate that part of the oil (above irreducible oil saturation) remains behind the water-oil front. This is a fundamental origin of low oil sweep efficiency during the process of immiscible oil displacement. Solutions of the Buckley-Leverett

equation in heterogeneous media (also neglecting capillary pressure) show that heterogeneities may "trap" oil (Wu et al., 1993; Kaasschieter, 1999), which is an additional reason for the low oil sweep efficiency. Analysis of the solutions in media with uniform permeability but heterogeneous capillary pressure revealed yet another mechanism of oil trapping (Kortekaas, 1985). The heterogeneities of various scales typical for the fluvial-type reservoirs add other complications to the process (Kjonsvik et al., 1994; Tye et al., 2003; Choi et al., 2011). The interplay of the different mechanisms makes oil sweep efficiency a complicated nonlinear function of the magnitude and direction of the pressure gradient (or velocity of the water-oil front) as well as the size, direction and connectivity of heterogeneities in capillary pressure and permeability. Indeed, as our simulations show, the spatial and temporal distribution of oil saturation in fluvial-type reservoirs critically depends on those parameters.

Corbett et al. (1992) modeled waterflooding in heterogeneous 2D reservoirs. They found that sweep efficiency in such reservoirs depends on the pressure gradient. The amount of oil recovered was different by a factor of two for different values of the pressure gradient. This effect was due to the difference in the capillary pressure in different materials leading to oil trapping in material with smaller capillary pressure. The amount of oil locally trapped depends on the pressure gradient (ΔP) and the size of heterogeneity in the gradient direction (l). If the difference in capillary pressure between two materials is small compared to $\Delta P^* l$, the effect of capillary pressure is also small. In contrast, if this difference is larger than $\Delta P^* l$, the trapping effect is dominant. Therefore, in our simulations, the trapping effect is larger for the smallest OFC clusters and there is no trapped oil in spanning OFC clusters (see Gershenzon et al., 2015; their Figs. 12 and 13). The opposite effect also occurs when oil from the material with large capillary pressure (sandstone in our case) is pushed by the capillary pressure into the material

with low capillary pressure (OFC). As a result, oil saturation in sandstone is reduced. The interplay between these two effects defines the spatial and temporal distribution of oil in a process of oil displacement by water. Thus, oil sweep efficiency is expected to depend on the pressure difference between injection and production wells, as has been concluded by Kortekaas (1985), Corbett et al. (1992), and Ringrose et al. (1993).

However, our analysis of simulations utilizing all six realizations revealed an unexpected result. In spite of the differences in the spatial distribution of oil for different pressure gradients, the integral parameters such as remaining oil saturation (hence oil sweep efficiency) did not depend on the pressure gradient (see Fig. 17). This was true regardless of the direction of the pressure gradient (i.e., parallel or normal to paleoflow direction). The effect of oil trapping in OFC clusters is offset by the effect of oil reduction from the surrounding sandstone. This effect occurred regardless of whether the OFC material formed limited or spanning clusters and even regardless of whether or not a spanning cluster occurred in the reservoir. Figs. 18 and 19 illustrate this result and support this conclusion. These Figs. show all cells within the reservoir having oil saturation in either of two different ranges at the same stage of the waterflooding process. Note that all cells with oil saturation in the range from 0.78 to 0.9 are the OFC cells because the irreducible saturation of the wetting phase (water) for the sandstone and OFC are different, at 0.22 and 0.1 respectively. These Figs. show that the total amount of OFC cells having such saturation of trapped oil is visibly different for the different pressure gradients for both realizations 1 and 6 (see top panels at Figs. 18 and 19). These Figs. show that the amount of trapped oil in OFC clusters is larger if the pressure gradient is smaller. In contrast, the amount of oil remaining in sandstone cells is smaller when the pressure gradient is smaller (bottom panels of Figs. 18 and 19).

CONCLUSIONS

The fluvial architecture represented here is not found in all reservoirs, but is found in some very important ones (e.g. the Ivishak Formation, Prudhoe Bay Field, Alaska, see, Stalkup et al, 1991; McGuire et al, 1994; McGuire et al, 1999; Tye et al., 2003). The basic model for hierarchical fluvial architecture used here (Lunt et al., 2004; Bridge 2006) is fairly general and applies over a broad range of median grain size. Furthermore, the dimensions of unit types across the stratal hierarchy scale together with the width of the channels forming the deposit (Bridge, 2006). An important characteristic of coarser-grained reservoirs is that open-framework conglomerate strata are connected and impart higher-permeability pathways within the reservoir (Tye et al., 2003; Guin et al., 2010). These pathways cannot be imaged in 2-D cross sections and their effect on the flow field cannot be understood from 2-D simulations (see Huang et al., 2012). To visualize and fully understand the impact of these connected flow pathways within a reservoir simulation requires advanced 3-D visualization tools as used here.

Several features distinguish our approach to reservoir simulation from others:

1) The modeled heterogeneity structure and scales, hence permeability distribution, realistically reflects the typical fluvial-type reservoirs.

2) The size of reservoir heterogeneities ranges from a few cm to dozens of meters.

3) The reservoir contains two different materials: sandstone and open-framework conglomerate. These materials have different properties, requiring two sets of property curves for simulation.

4) Capillary pressure effects are utilized in the simulations.

By directly representing the smaller-scale cross-sets and their organization within bar deposits, the results allow a direct study of how they influence oil trapping processes and hence the oil sweep efficiency. The OFC cross-sets form connected clusters of different sizes, but as organized within bar deposits, the clusters typically have a larger extent in the paleoflow direction. This anisotropy affects the integral parameters of waterflooding such as water breakthrough time, cumulative oil production and oil sweep efficiency. Fingering on the water-oil boundary might be expected because of the large difference in permeability between OFC and sandstone, the size of some of the OFC clusters may considerably exceed the cell size in both horizontal and vertical directions, and the majority of oil reaches the production wells through OFC channels. However, large-scale (with typical scale much larger than horizontal cell size) fingering was not observed. We did observe different degrees of water-oil front diffusivity for the different reservoir realizations and different pressure gradients, which could be considered as small-scale fingering. Large-scale fingering is absent because the width in vertical direction of the sandstone layers between OFC channels is small, so there is enough time for oil to diffuse from the sandstone to OFC channels, unless the pressure gradient is extremely large.

The content, structure and connectivity of high permeability material in a fluvial reservoir affects both oil production rate and water breakthrough time. However, oil sweep efficiency is not practically affected by the proportion and degree of connectivity of high-permeability beds. The most surprising finding of our 3D simulations is the independence of oil sweep efficiency from the pressure gradient in all considered realizations and directions of the pressure gradient. This is even more surprising if we keep in mind the highly nonlinear character of waterflooding processes. The amount of oil trapped in OFC, which decreases with increase of pressure gradient, is compensated by the amount of remaining oil in sandstone, which increases with

increase of pressure gradient, in such a way that the total amount of remaining oil does not depend on the pressure gradient. This "self-regulating process" could be understood in terms of small-scale and dense networks of OFC cells. Thus, oil sweep efficiency is not affected by the pressure gradient although the spatial distribution of residual oil critically depends on this value.

ACKNOWLEDGMENTS

We thank Schlumberger Company for donation of ECLIPSE Reservoir Simulation Software and the Ohio Supercomputer Center for allocations of processor time and technical support. We also thank the Editor Lesli Wood, reviewer Robert Tye and anonymous reviewer for useful comments and suggestions. The RVA visualization software was developed through support from the US Department of Energy National Energy Technology Laboratory under contract DE-FE0005961.

REFERENCES CITED

Bridge, J.S., 2006, Fluvial facies models: Recent developments, in Facies Models Revisited, SEPM Spec. Publ., 84, edited by H. W. Posamentier and R. G. Walker, Soc. for Sediment. Geol. (SEPM), Tulsa, Okla, p. 85–170.

Buckley, S.E., Leverett, M.C., 1942, Mechanism of Fluid Displacement in Sands, AIME Transactions, v. 146, p. 107–116.

Choi, K., Jackson, M.D., Hampson, G.J., Jones, A.D.W. , Reynolds, A. D., 2011, Predicting the impact of sedimentological heterogeneity on gas–oil and water–oil displacements: fluvio-deltaic

Pereriv Suite Reservoir, Azeri–Chirag–Gunashli Oilfield, South Caspian Basin, Petroleum Geoscience, v. 17, p. 143–163, doi:10.1144/1354-079310-013.

Conrad, C. M., Ritzi, R. W., Dominic, D. F., 2008, Air-based measurements of permeability in pebbly sands, Groundwater, v.46, no.1, p.103-112.

Corbett, P.W.M., Ringrose, P.S., Jensen, J.L., Sorbie, K.S., 1992, Laminated Clastic Reservoirs: The Interplay of Capillary Pressure and Sedimentary Architecture, SPE Annual Technical Conference and Exhibition, 4-7 October 1992, Washington, D.C., doi: 10.2118/24699-MS.

Gershenzon, N. I., Soltanian, M., Ritzi Jr, R. W., & Dominic, D. F., 2015, Understanding the Impact of Open-Framework Conglomerates on Water-Oil Displacements: Victor Interval of the Ivishak Reservoir, Prudhoe Bay Field, Alaska, Petroleum Geoscience v. 21, p. 43–54.

Gharbi, R.B., E.J. Peters, Garrouch, A.A., 1997, Effect of heterogeneity on the performance of immiscible displacement with horizontal wells, Journal of Petroleum Science and Engineering v. 18, p. 35-47.

Guin, A., Ritzi, R.W., 2008, Studying the effect of correlation and finite-domain size on spatial continuity of permeable sediments, Geophysical Research Letters, v**.** 35**,** no. 10, *p.* 1–7, doi: 10.1029/2007GL032717.

Guin, A., Ramanathan, R., Ritzi, R.W., Dominic, D.F., Lunt, I.A., Scheibe, T.D., Freedman, V.L., 2010, Simulating the heterogeneity in braided channel belt deposits: 2. Examples of results and comparison to natural deposits, Water Resour. Res., v. 46, W04516, 1-19, doi:10.1029/2009WR008112.

Huang, L., Ritzi, R.W., Ramanathan, R., 2012, Conservative models: parametric entropy vs. temporal entropy in outcomes, Ground Water , v.50, no. 2, p.199–206, doi: 10.1111/j.1745-6584.2011.00832.x.

Jones, A., Doyle, J., Jacobsen, T., Kjonsvik, D., 1995, Which sub-seismic heterogeneities influence waterflood performance? A case study of a low net-to-gross fluvial reservoir, in De Haan, H. J.,e d., New Developments in Improved Oil Recovery, Geological Society Special Publication, no. 84, p. 5-18.

Kaasschieter, E.F., 1999, Solving the Buckley-Leverett Equation with Gravity in a Heterogeneous Porous Medium, Computational Geosciences, v. 3, no. 1, p. 23-48.

Keefer, D., Torridi, D., Duggirala, J., 2012, RVA: Reservoir Visualization and Analysis: User Manual, Illinois State Geological Survey, University of Illinois, Urbana-Champaign, 46 pp.

Khataniar, S., Peters, E. J., 1992, The effect of reservoir heterogeneity on the performance of unstable displacements, Journal of Petroleum Science and Engineering, v. 7, p. 263-281.

524 Kjonsvik, D., Doyle, J., Jacobsen,T., Jones, A., 1994, The Effects of Sedimentary
525 Heterogeneities on Production from a Shallow Marine Reservoir - What Really Matters? ,Society
526 of Petroleum Engineers, p. 27-40, doi: 10.2118/28445-MS.
527
528 Klingbeil, R., Kleineidam, S., Asprion, U., Aigner, T., Teutsch, G., 1999, Relating lithofacies to
529 hydrofacies: outcrop-based hydrogeological characterization of quaternary gravel deposits.
530 Sedimentary Geology, v.129, p.299– 310.
531
532 Kortekaas, T.F.M., 1985, Water/Oil Displacement Characteristics in Cross bedded Reservoir
533 Zones, Society of Petroleum Engineers, v. 25, no. 6, doi:10.2118/12112-PA.
534
535 Lunt, I.A., Bridge, J.S., Tye, R.S., 2004a, A quantitative, three dimensional depositional model
536 of gravelly braided rivers, Sedimentology, v. 51, no 3, p. 377–414, doi:10.1111/j.1365-
537 3091.2004.00627.x.
538
539 Lunt, I.A., Bridge, J.S. and Tye, R.S. (2004b) Development of a 3-D depositional model of
540 braided river gravels and sands to improve aquifer characterization. In: Aquifer Characterization
541 (Eds J.S. Bridge and D.W. Hyndman), SEPM Spec. Publ. 80.
542
543 Lunt, I.A., Bridge, J.S., 2007, Formation and preservation of open-framework gravel strata in
544 unidirectional flows, Sedimentology, v. 54, p. 71–87, doi:10.1111/j.1365-3091.2006.00829.x.
545

McGuire, P.L., Spence, A.P., Stalkup, F.I., Cooley, M.W., 1994, Core acquisition and analysis for optimization of the Prudhoe Bay miscible gas project, 9th Society of Petroleum Engineers/Department of Energy Symposium on Improved Oil Recovery, Tulsa, Oklahoma, no. 27759, p. 253–265.

McGuire, P.L., Redman, R.S., Mathews, W.L., Carhart, S.R., 1999, Unconventional Miscible EOR Experience at Prudhoe Bay, SPE, v. 2, no 3, p. 222-229. doi: 10.2118/56849.

McGuire, P. L., R. S. Redman, W. L. Mathews, and S. R. Carhart, 1999, Unconventional miscible EOR Experience at Prudhoe Bay: Journal of Petroleum Technology, v. 51, no. 1, p. 38–41.

Ramanathan, R., Guin, A., Ritzi, R.W., Dominic, D.F., Freedman, V.L., Scheibe, T.D., Lunt, I.A., 2010, Simulating the heterogeneity in channel belt deposits: Part 1. A geometric-based methodology and code, Water Resources Research, v. 46, W04515. doi:10.1029/2009WR008111.

Ringrose, P., Sorbie, K., Corbett, P., Jensen, J., 1993, Immiscible Flow Behaviour in Laminated and Cross-Bedded Sandstones, Journal of Petroleum Science and Engineering, v. 9, no. 2, p.103-124.

Rose, S.C., J.F. Buckwalter, and R.J. Woodhall, 1989, The Design Engineering Aspects of Waterflooding, SPE Monograph Series, Voume 11, Richardson, TX

Stalkup, F. I., and S. D. Crane, 1991, Reservoir description detail required to predict solvent and water saturations at an observation well, Paper No. 22897: 66th Annual Society of Petroleum Engineers Technical Conference and Exhibition, Dallas, Texas, p. 151–164.

Tye, R. S., Watson, B. A., McGuire, P. L., Maguire, M. M., 2003, Unique horizontal-well designs boost primary and EOR production, Prudhoe Bay field, Alaska, in T. R. Carr, E. P. Mason, and C. T. Feazel, eds., Horizontal wells: Focus on the reservoir, AAPG Methods in Exploration , no. 14, p. 113–125.

Wu, Y.S., Pruess, K., Chen, Z.X., 1993, Buckley-Leverett Flow in Composite Porous Media, SPE J., v. 1, no. 2, p. 36-42, doi: 10.2118/22329-PA.

Figure captions

Figure 1. (Top) Aerial photograph of the portion of the Sagavanirktok River studied by Lunt et al., (2004) with the active channel belt and the preserved channel belt deposits identified.. (Middle and Bottom) Conceptual model for the hierarchical sedimentary architecture found in channel belt deposits (Lunt et al., 2004) (see also Table 1). The compound bar deposits (level III) result from the processes of unit-bar accretion and channel migration. Within unit bar deposits (level II), sets of open-framework gravel (level I) have the highest permeability. As channels are abandoned, they are filled with lower-permeability sediment. Major channel fills (level III) and smaller cross-bar channel fills (level II) are lower-permeability baffles within the deposit. From Ramanathan et al. (2010).

Figure 2. Steps in creating the geometric and geocellular models. (a) Creating an archetypal polyhedron with piecewise-planar elements. The archetypal polyhedron is formed from a parsimonious number of input geometric lengths drawn from statistical distributions. The polyhedron initially has a straight centerline. (b) Adding curvature to the centerline. (c) Merging with other unit types according to rules of deposition. In the same way, cross-set polyhedra are created and fill the unit bars, etc. (not shown). In a second step, a geocellular (digital) model (c) is created on a regular voxel grid of any desired resolution. (d) Only pieces of the archetypal unit bars are preserved in the geometric and geocellular models of the preserved deposit.

Figure 3. (Top) Exposure of channel belt deposits in a trench at the Sagavanirktok River field site (from Lunt, 2002). (Bottom) Rendering of an extracted piece of a geometric model produced using the approach illustrated in Fig. 2. View is oblique but nearly parallel to paleoflow direction. Boundaries of unit types have been given an orange color to distinguish individual unit bar deposits and cross-set boundaries (thickness of the boundary is arbitrary). No vertical exaggeration.

Figure 4. Distribution of sandstone (red) and OFC (blue) in realizations 6 (16% of OFC; top panel), 4 (22% of OFC; panel in the middle) and 1 (28% of OFC; bottom panel). Paleoflow is from right to left. The reservoir size is 200:200:5 m. Vertical exaggeration is 10X.

Figure 5a. Distribution of OFC in realizations 6 (16% of OFC; top panel), 4 (22% of OFC; panel in the middle) and 1 (28% of OFC; bottom panel). The reservoir size is 200:200:5 m (100:100:100 cells). Vertical exaggeration is 10X.

615

616 **Figure 5b**. The distribution of OFC in portions of the realizations shown in Fig. 5a. The domain
617 shown is 50:50:1.25 m (25:25:25 cells).

618

619 **Figure 6**. The five largest clusters of OFC in realization 4 (proportion of OFC is 22%) are
620 depicted after extracting them from the entire volume. The largest cluster spans the entire
621 domain (i.e. is a spanning cluster) and is approximately 200:200:5 m (100:100:100 cells).

622

623 **Figure 7**. Image of reservoir with 16% (top) and 28% (bottom) of OFC. Panels on the left show
624 distribution of sandstone (red) and OFC (blue) and panels on the right show the corresponding
625 permeability.

626

627 **Figure 8a**. Images of permeability map for the realization of reservoir with 28% of OFC. Each
628 image shows all cells with permeability in the range indicated at the top of the image. The
629 percentage of cells with permeability in specified range from the total cell number is also shown.

630

631 **Figure 8b**. The same as Figure 8a for the realization of reservoir with 16% of OFC.

632

633 **Figure 9**. Capillary pressure and relative permeability of oil and water versus water saturation
634 for sandstone and OFC lithotypes.

635

636 **Figure 10**. Oil saturation distribution in reservoir realization 4 after 200 days of water injection.
637 Pressure difference between wells is 100 psi. Paleoflow was left to right in the top panel and

front to back in the lower panel. Pressure gradient is parallel (top panel) and normal (bottom panel) to paleoflow direction. The wells are perforated along total reservoir width.

Figure 11. Oil (solid line) and water (dashed line) production rates v. time for realization 3. The pressure difference between the injector and producer wells is 200 psi and the pressure gradient is along the *y* direction.

Figure 12. Oil and water production rates v. injected water volume for the six modelled realizations (Table 1) (the proportion of OFC is shown at the top right-hand corner of each graph). The pressure difference between the injector and producer wells is 200 psi. The solid lines show the oil production rates when the pressure gradient is along the *y* direction; dashed lines show the water production rates when the pressure gradient is along the *y* direction; dot-dashed lines show the oil production rates when the pressure gradient is along the *x* direction; dotted lines show the water production rates when the pressure gradient is along the *x* direction. The injected water volume is normalized by the pore volume of the reservoir minus the irreducible water volume and residual oil saturation. From Gershenzon et al, (2015).

Figure 13. Animated oil saturation distribution in reservoir realization 4 from the beginning of water injection up to 500 days. Pressure difference between wells is 100 psi, pressure gradient is parallel (a) and normal (b) to paleoflow (y) direction.

Figure 14. View of all (but spanning) OFC clusters (total number of clusters is 8562) extracted from the 200:200:5 m domain of realization 4. Most of the clusters are elongate in paleoflow (*y*)

direction. Clusters are arbitrarily assigned different colors. The white arrow shows paleoflow direction.

Figure 15. Oil saturation distribution for the slices of reservoir 0:200 x 100:160 x 1:5 m for the realization 1 (bottom panels) and 6 (top panels). Pressure difference between wells is 100 psi (left panels) and 800 psi (right panels). 16% and 28% indicate the percentage of OFC.

Figure 16. Image of oil migration paths in fluvial-type reservoirs during waterflooding.

Figure 17. Oil saturation averaged over OFC cells (blue), sandstone cells (green) and all cells (red) after injection of 1 water volume (in units of pore space volume minus volume of connate water and volume of irreducible oil) as function of pressure difference for realization #5. From Gershenzon et al, (2015).

Figure 18. Cells with oil saturation in the range indicated at the top of each panels for the reservoir realization 6 (16% of OFC) after waterflooding with pressure difference between injection and production wells of 100 psi (panels at the left) and 800 psi (panels at the right). The choice of intervals of oil saturation is arbitrary, i.e. 0.49-0.5 for sandstone and 0.8-0.9 for OFC. The intervals were chosen to make the effect more visible. The scale is 200:200:5 m.

Figure 19. The same as at Fig. 18 for the reservoir realization 1 (28% of OFC).

Figure 1
Click here to download Figure: Figure 1.tif

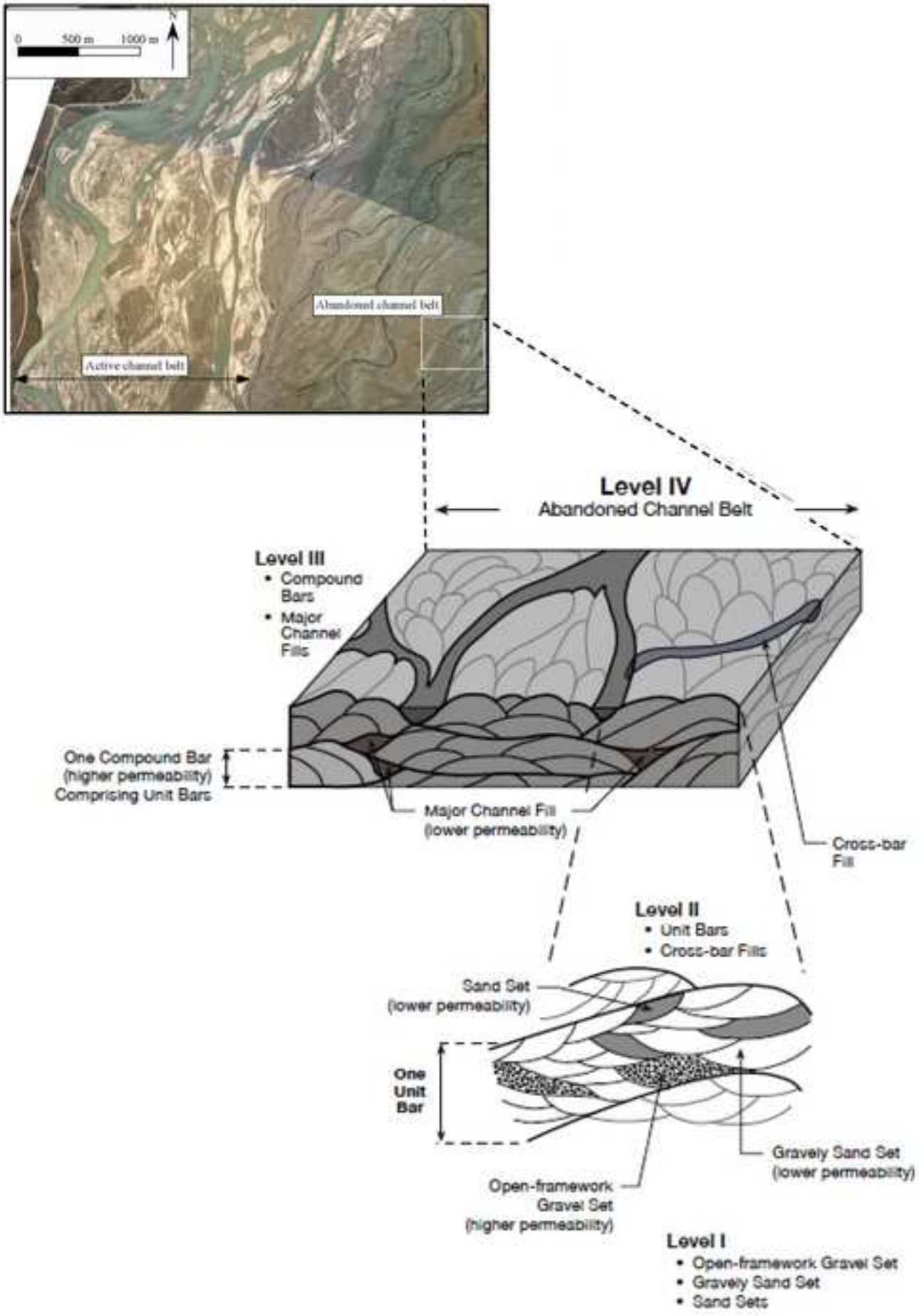

Figure 2
Click here to download Figure: Figure 2.tif

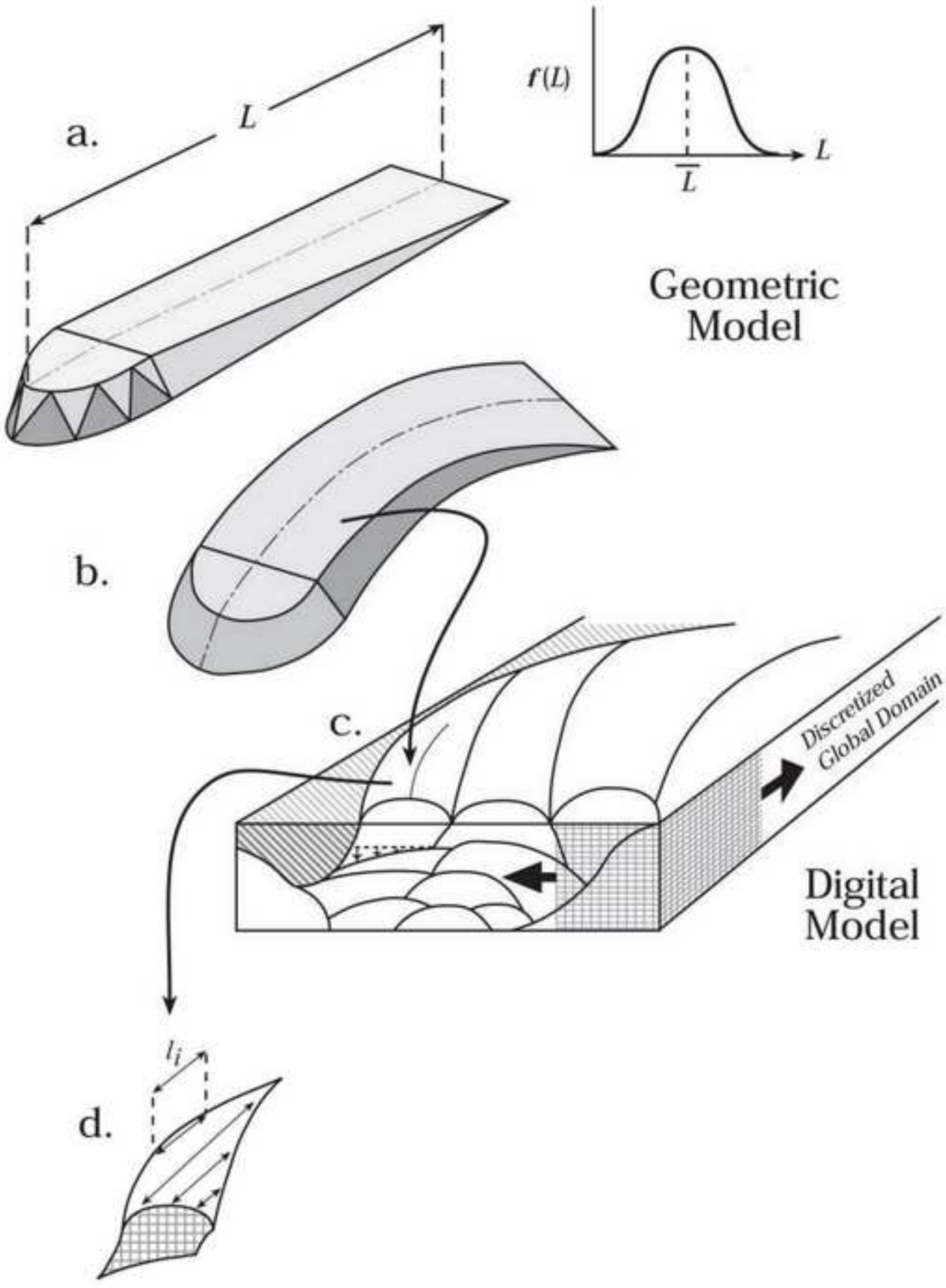

Figure 3
Click here to download Figure: Figure 3.tif

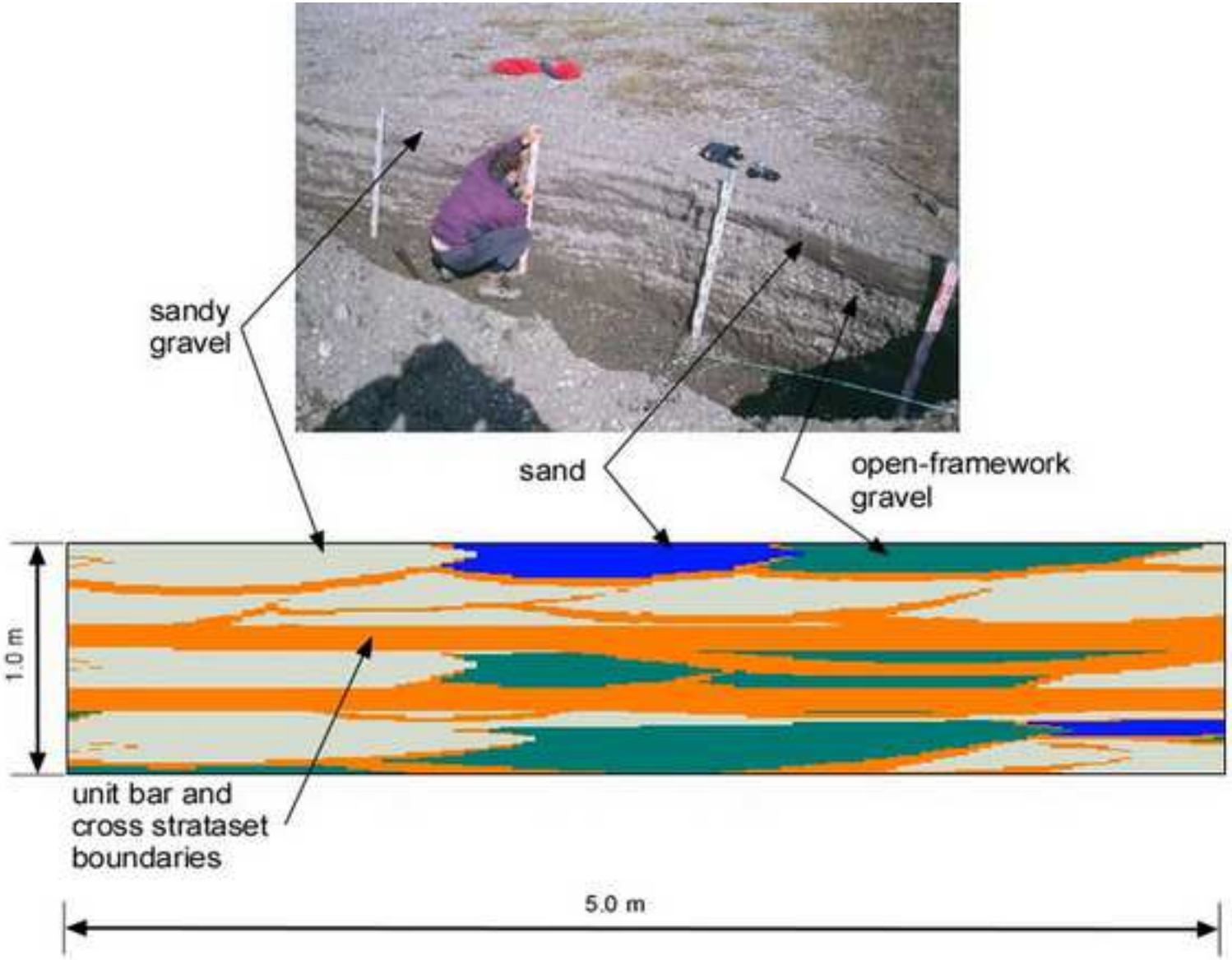

Figure 4
Click here to download Figure: Figure 4.tif

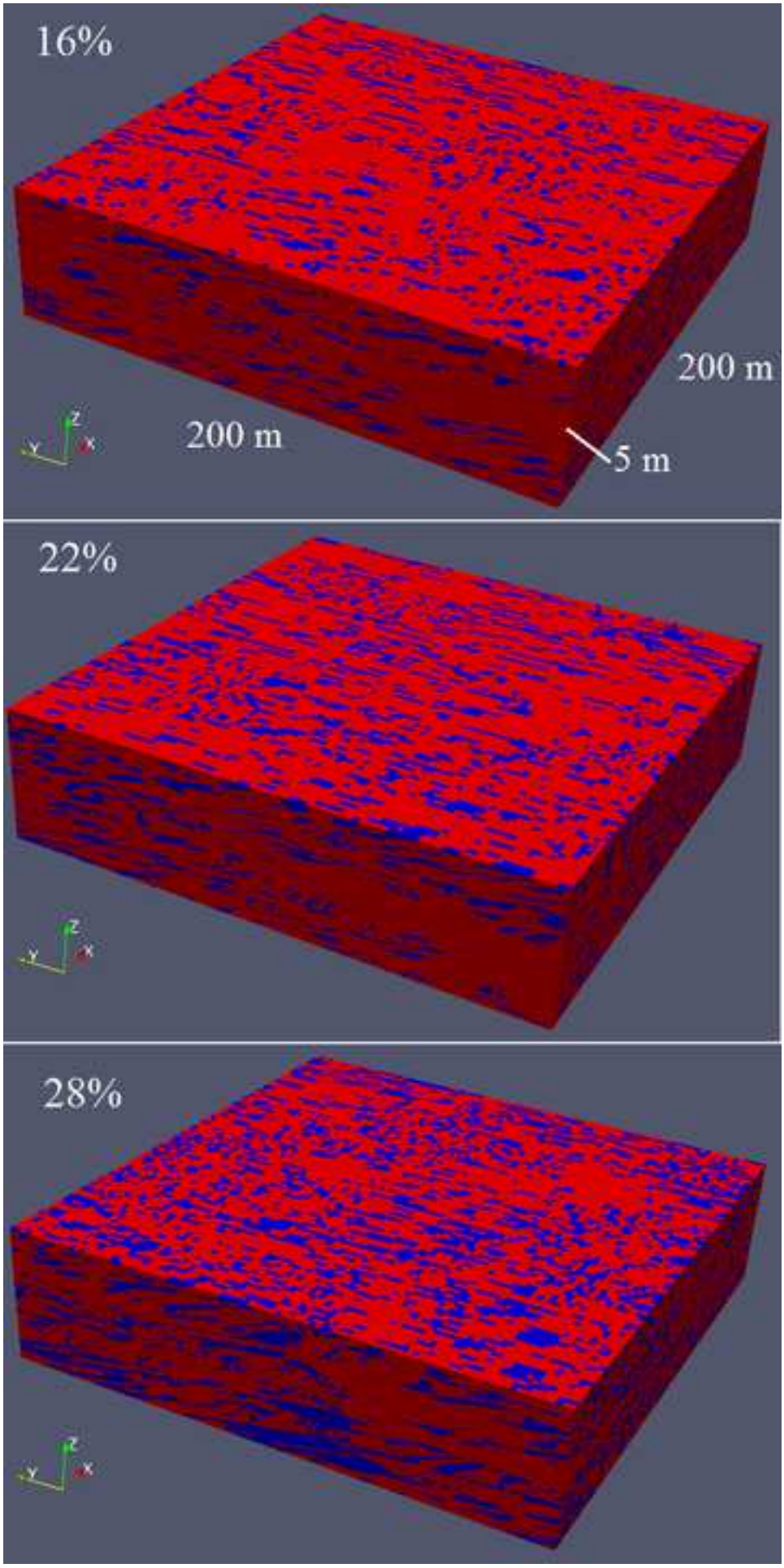

Figure 5a
Click here to download Figure: Figure 5a.tif

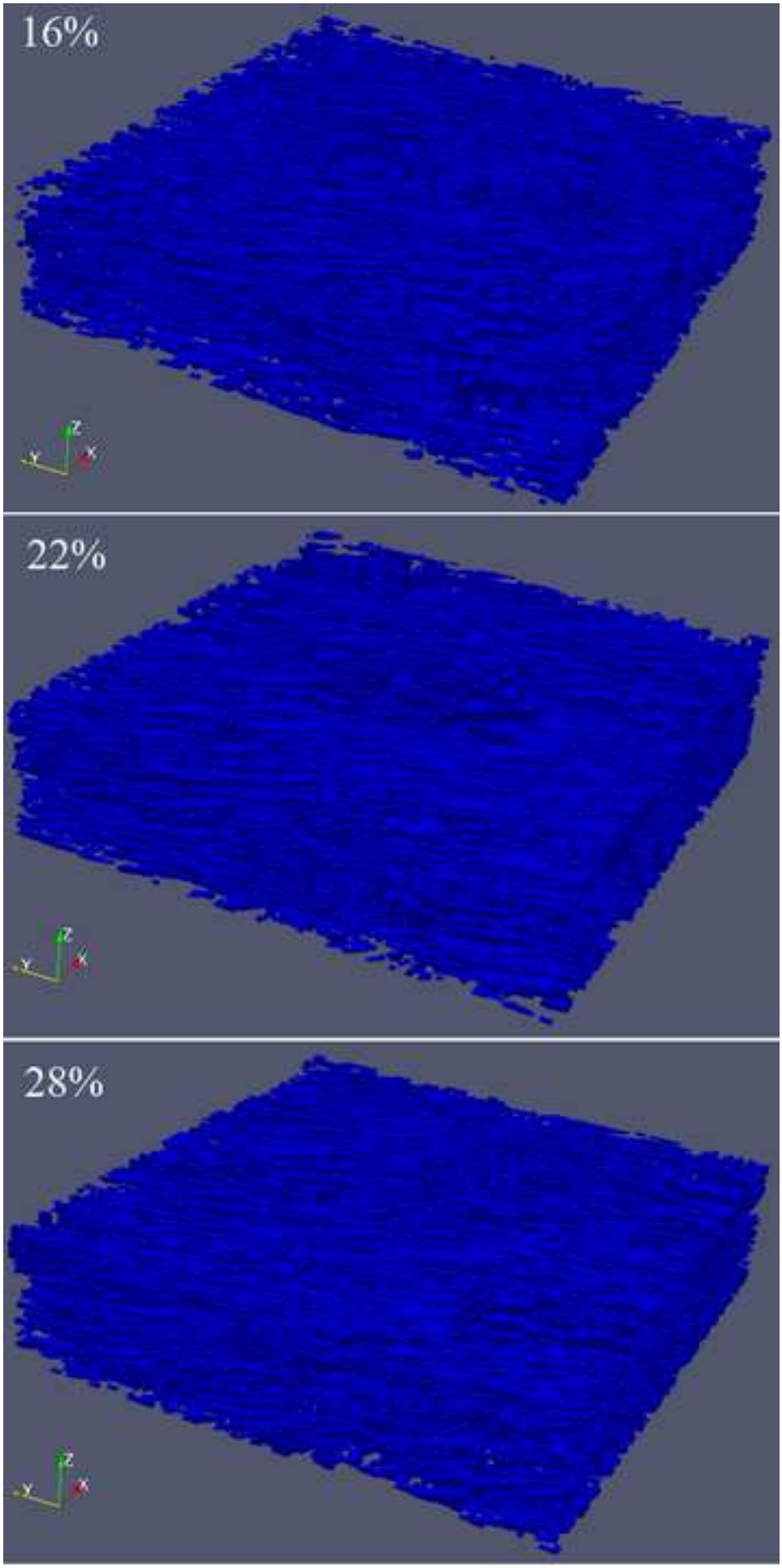

Figure 5b
Click here to download Figure: Figure 5b.tif

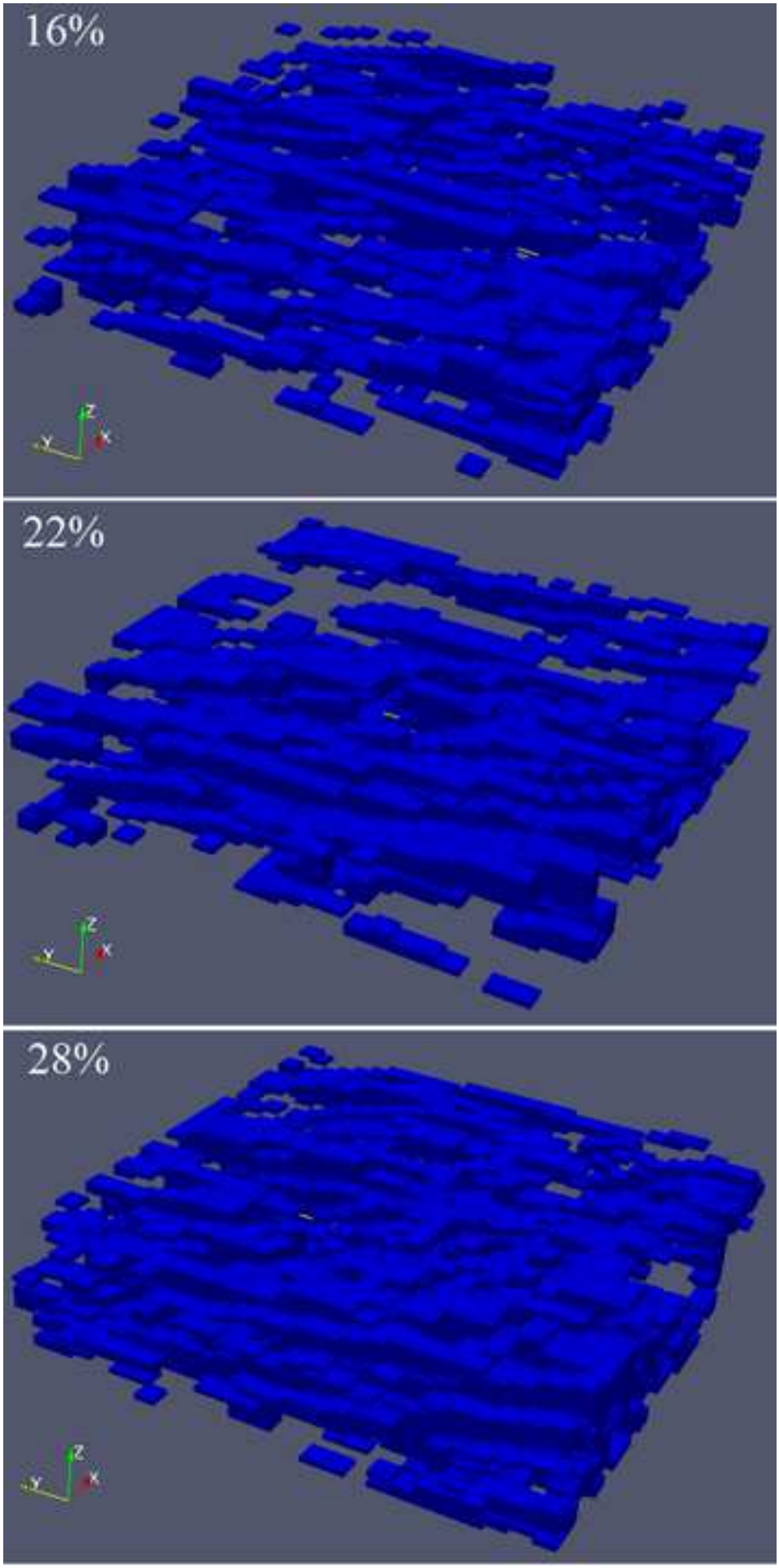

Figure 6
Click here to download Figure: Figure 6.tif

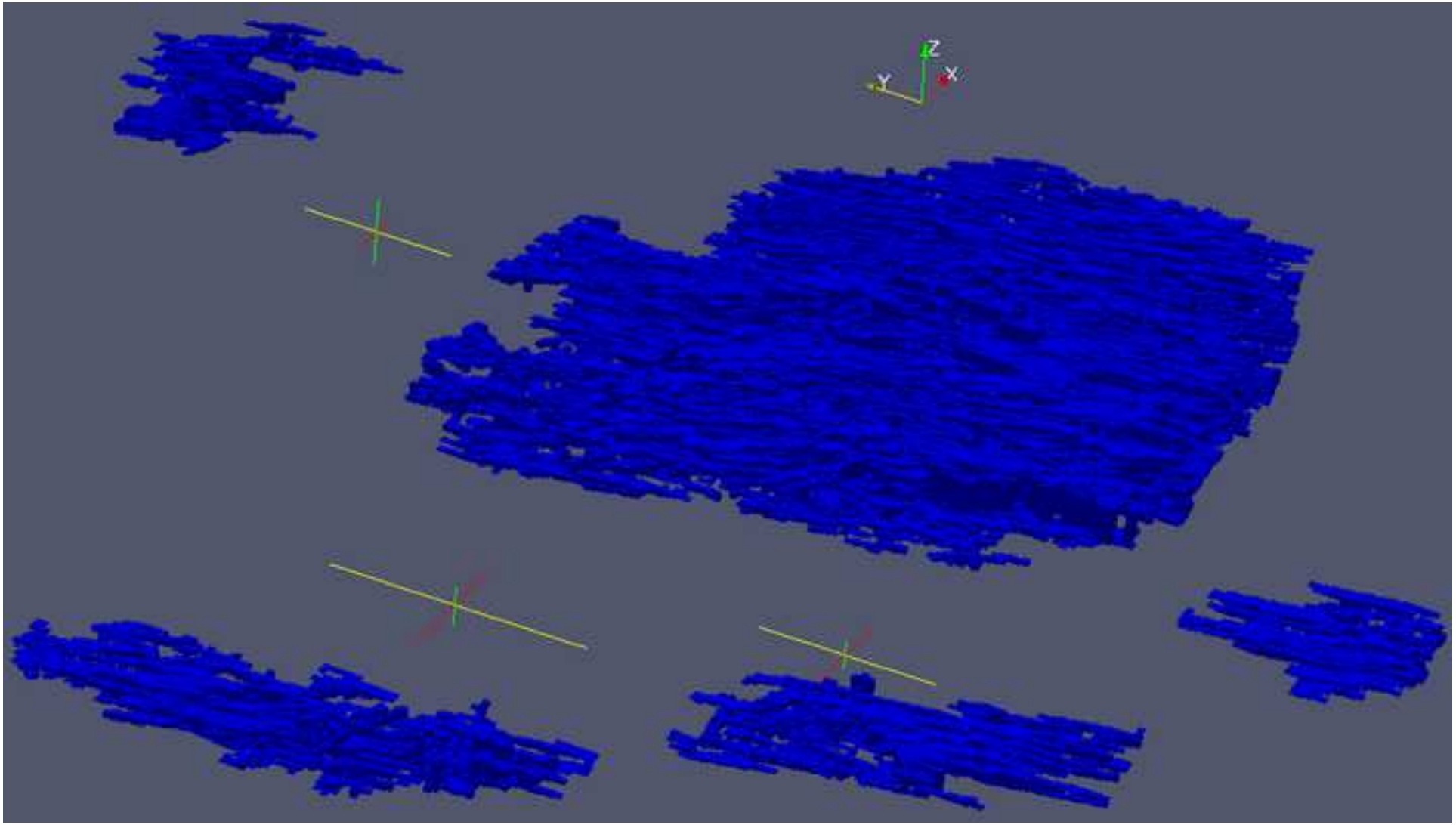

Figure 7
Click here to download Figure: Figure 7.tif

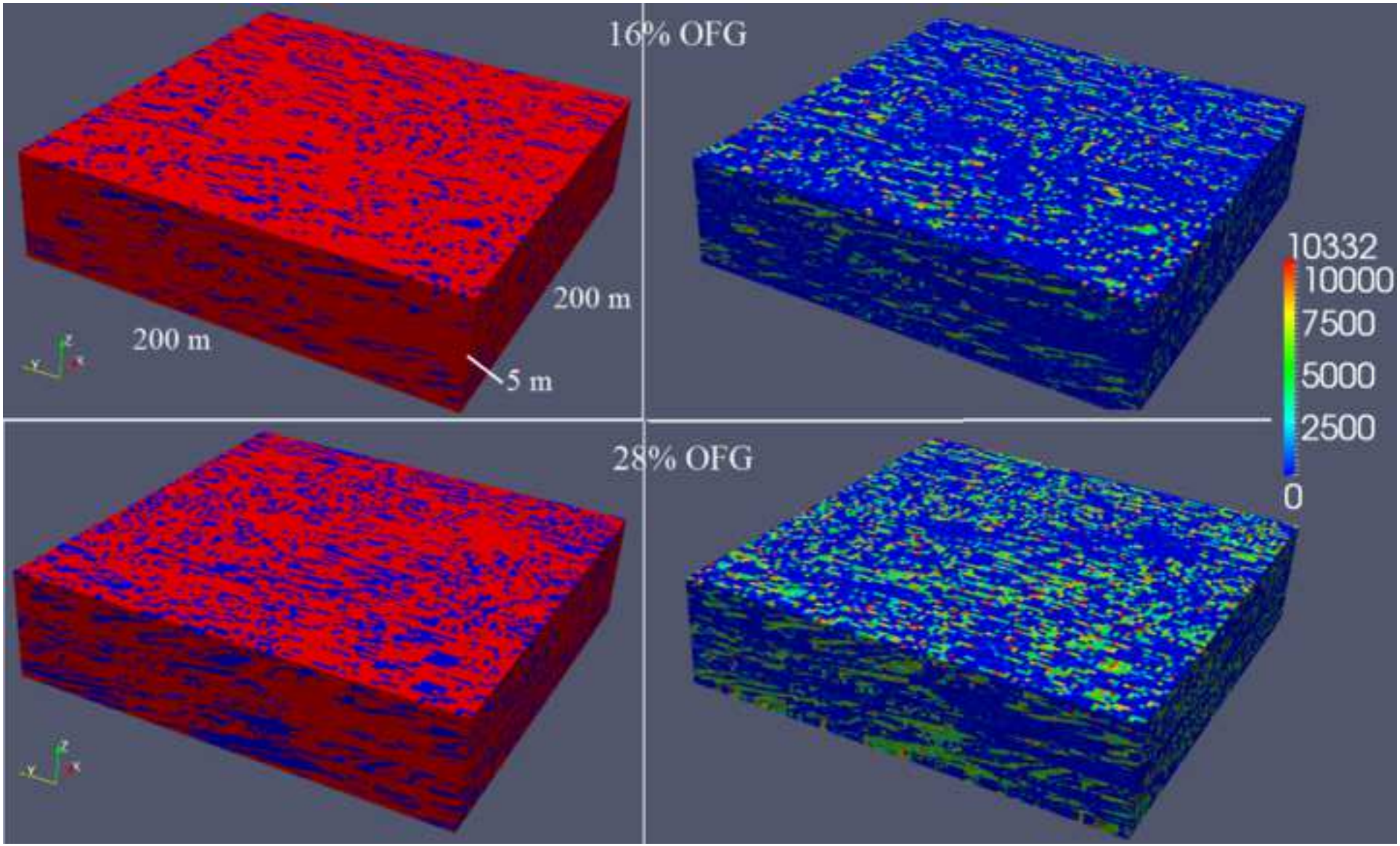

Figure 8a
Click here to download Figure: Figure 8a.tif

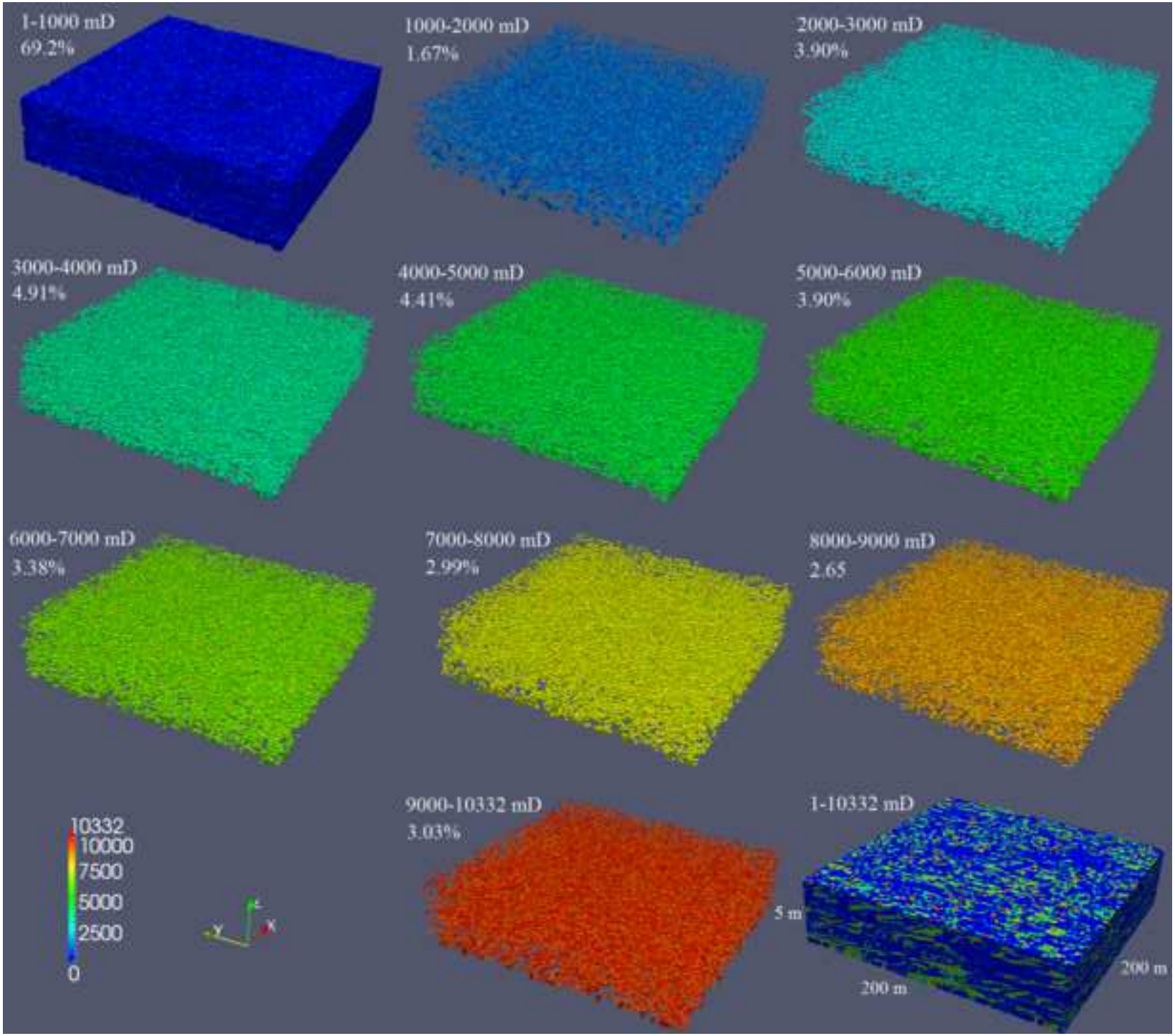

Figure 8b
Click here to download Figure: Figure 8b.tif

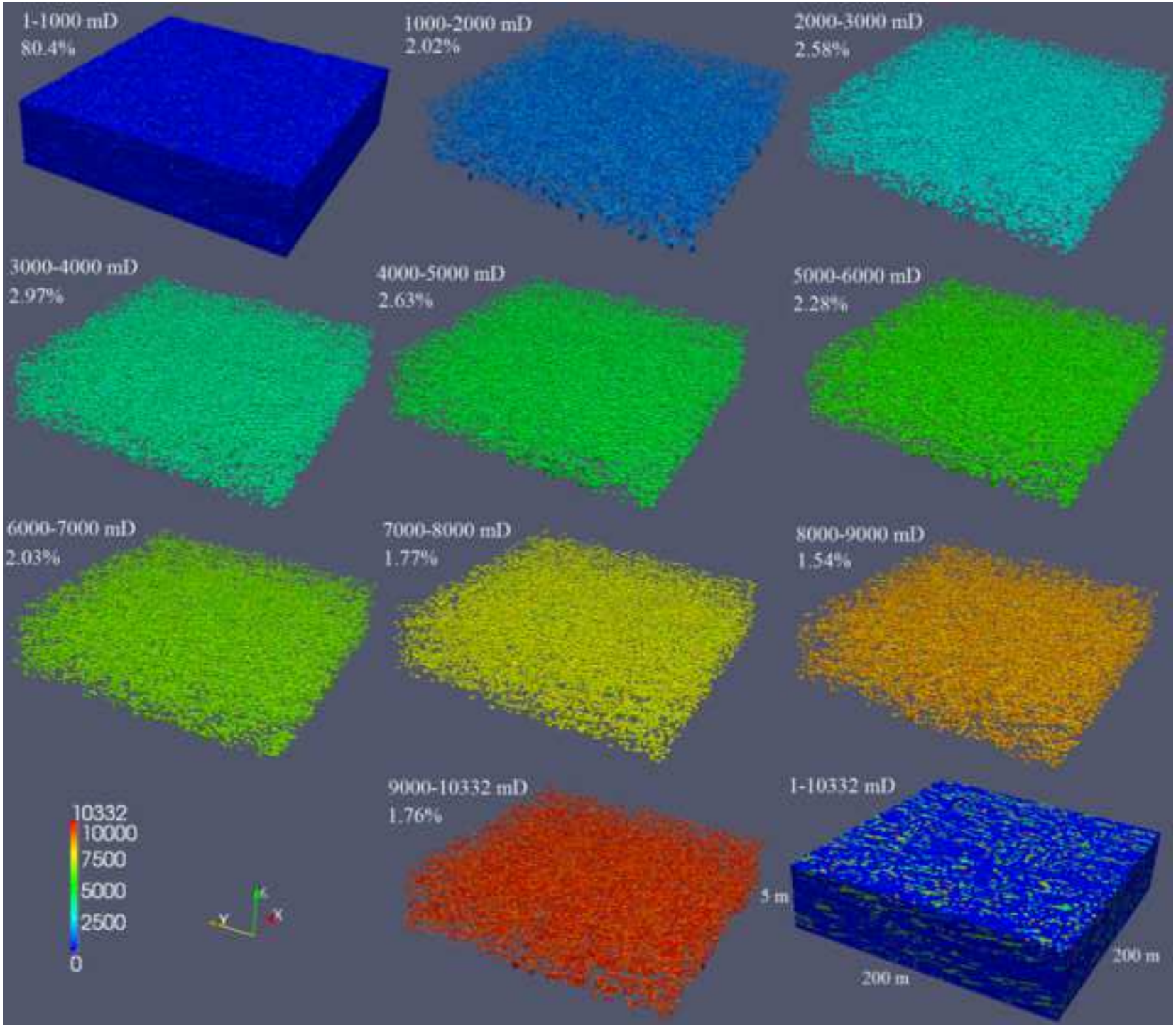

Figure 9
Click here to download Figure: Figure 9.tif

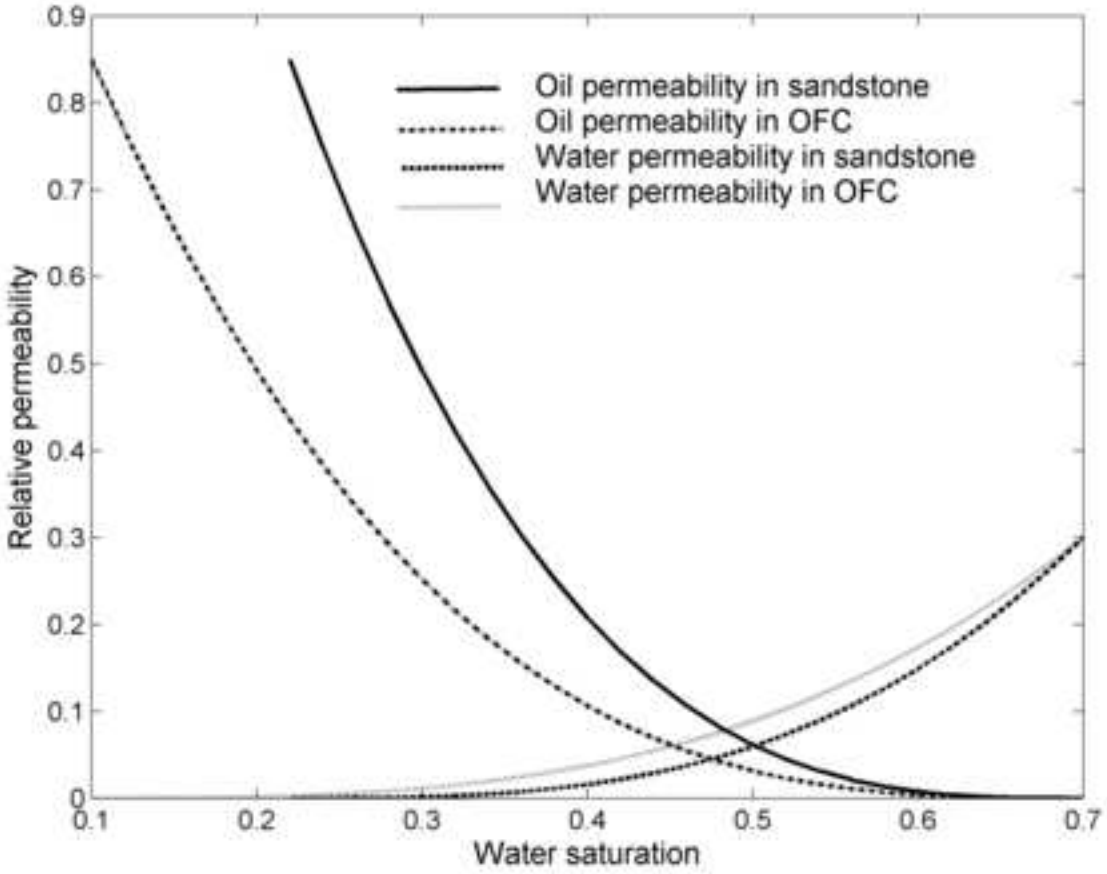

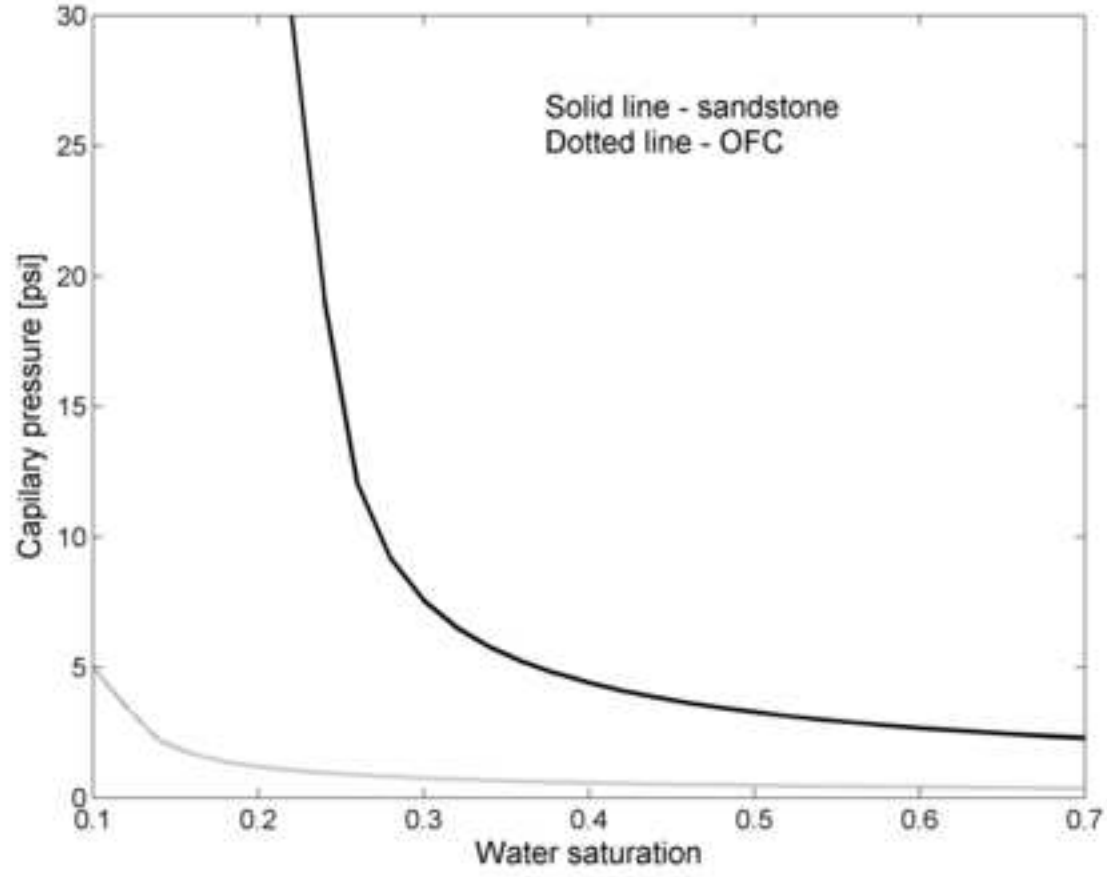

Figure 10
Click here to download Figure: Figure 10.tif

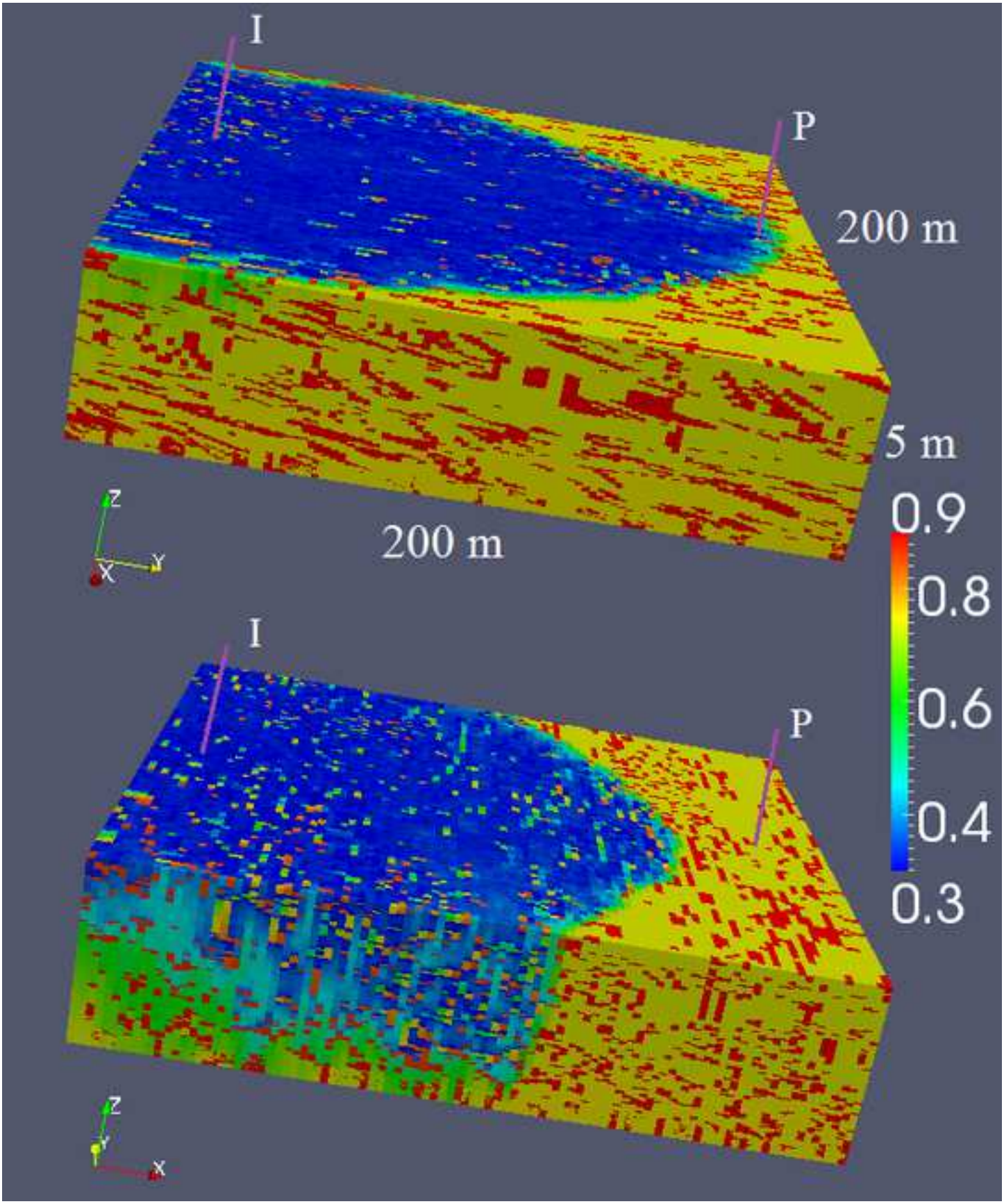

Figure 11
Click here to download Figure: Figure 11.tif

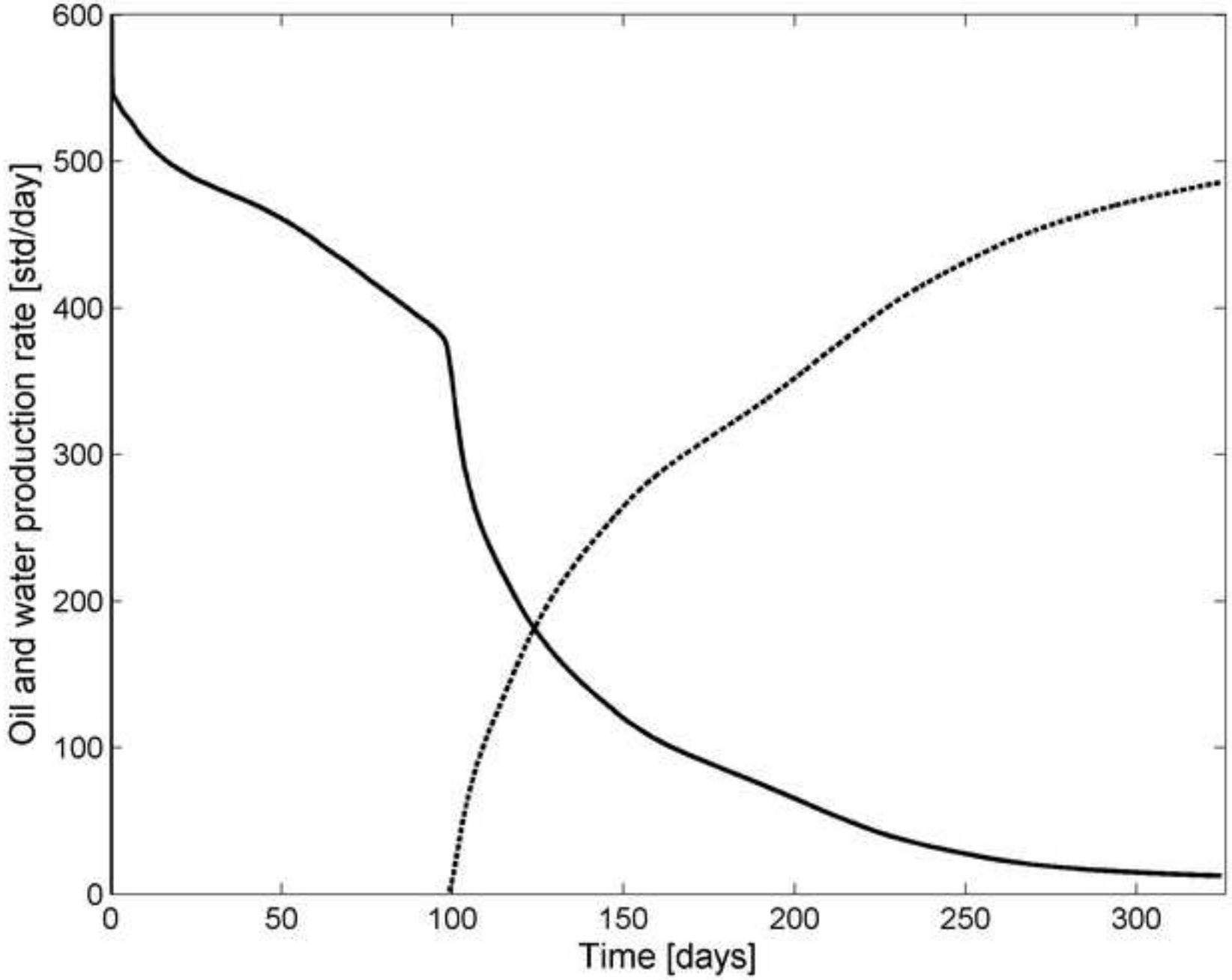

Figure 12
Click here to download Figure: Figure 12.tif

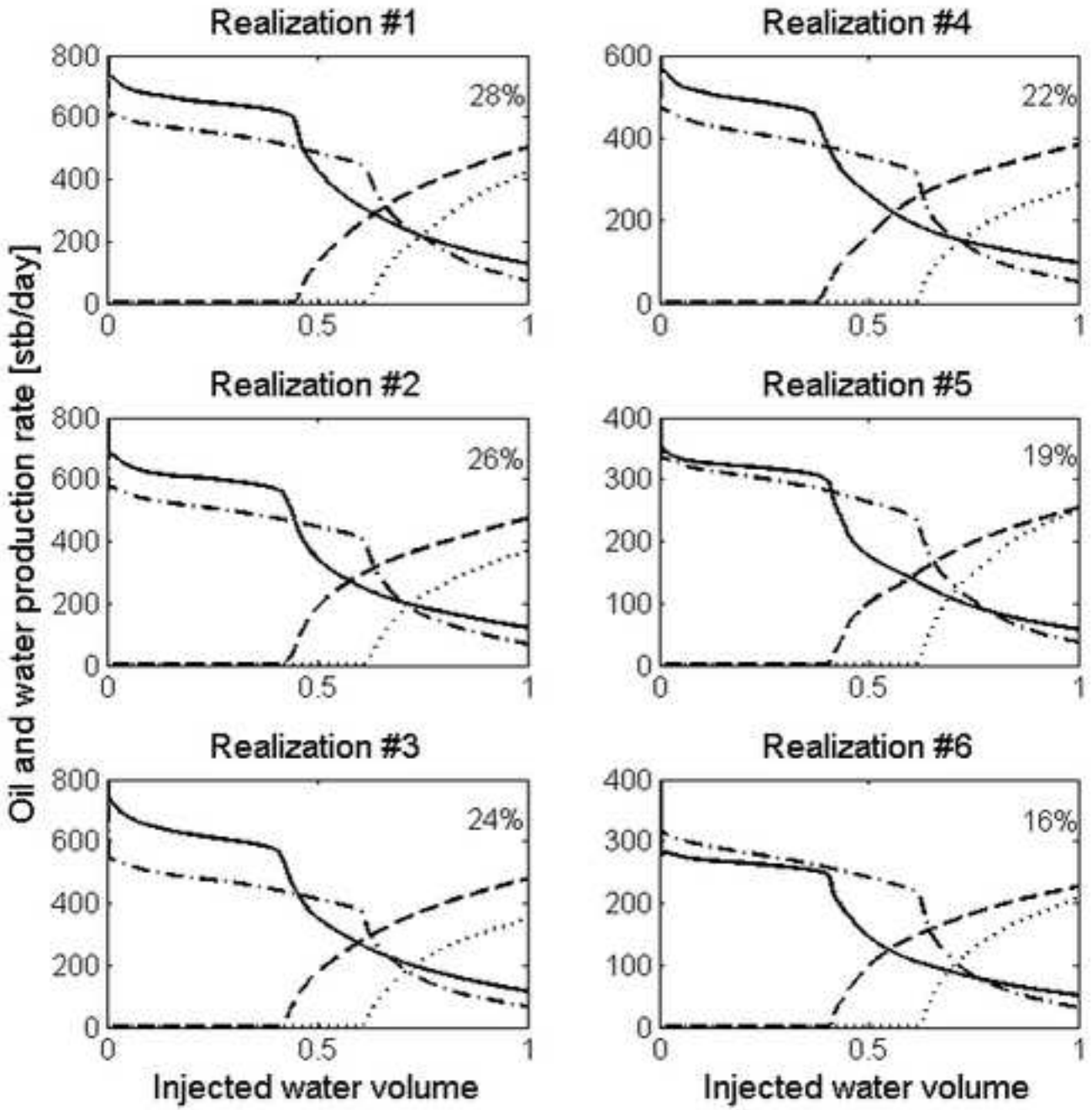

Figure 13 (animated)
Click here to download Supplemental file: Figure 13.avi

Figure 14
Click here to download Figure: Figure 14.tif

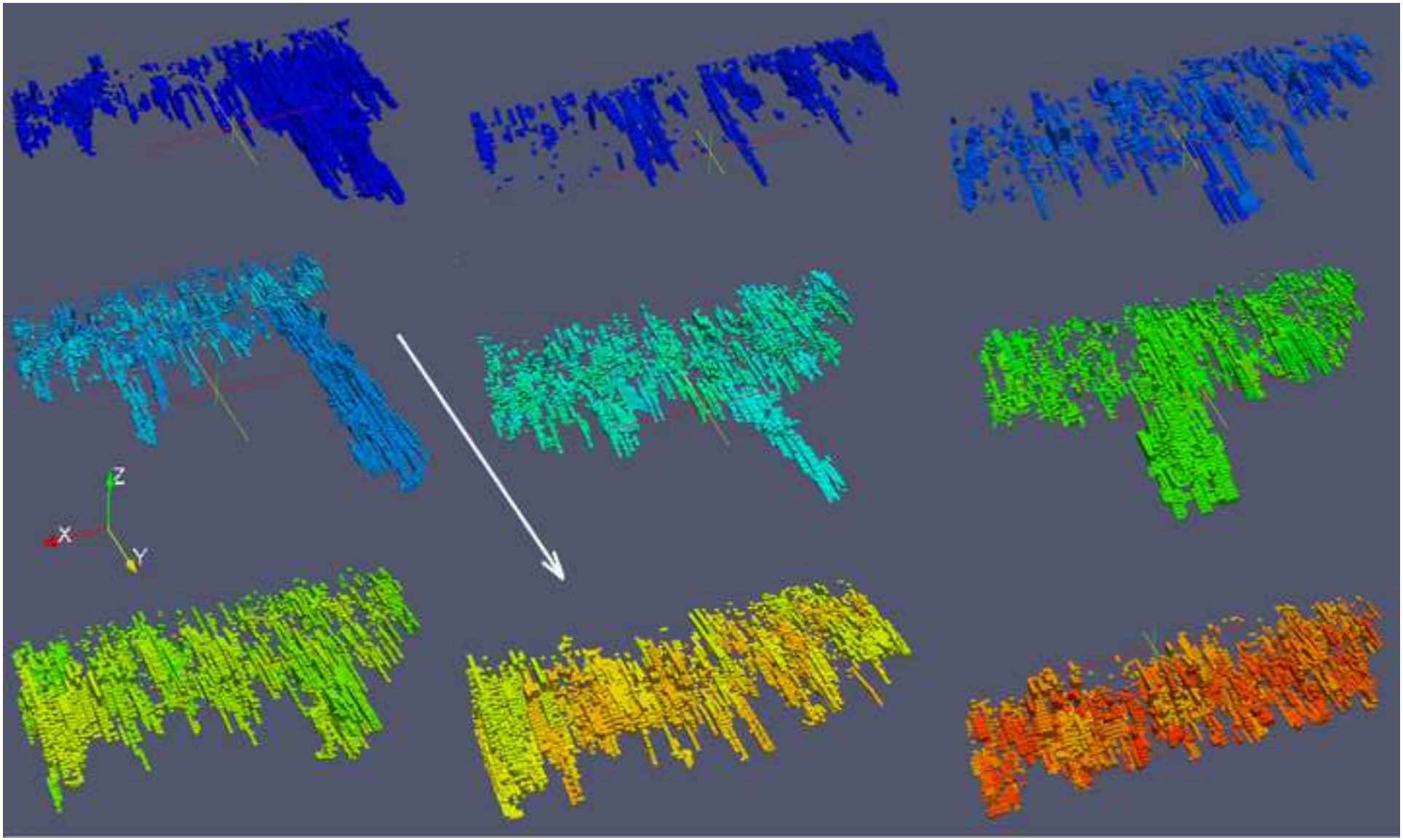

Figure 15
Click here to download Figure: Figure 15.tif

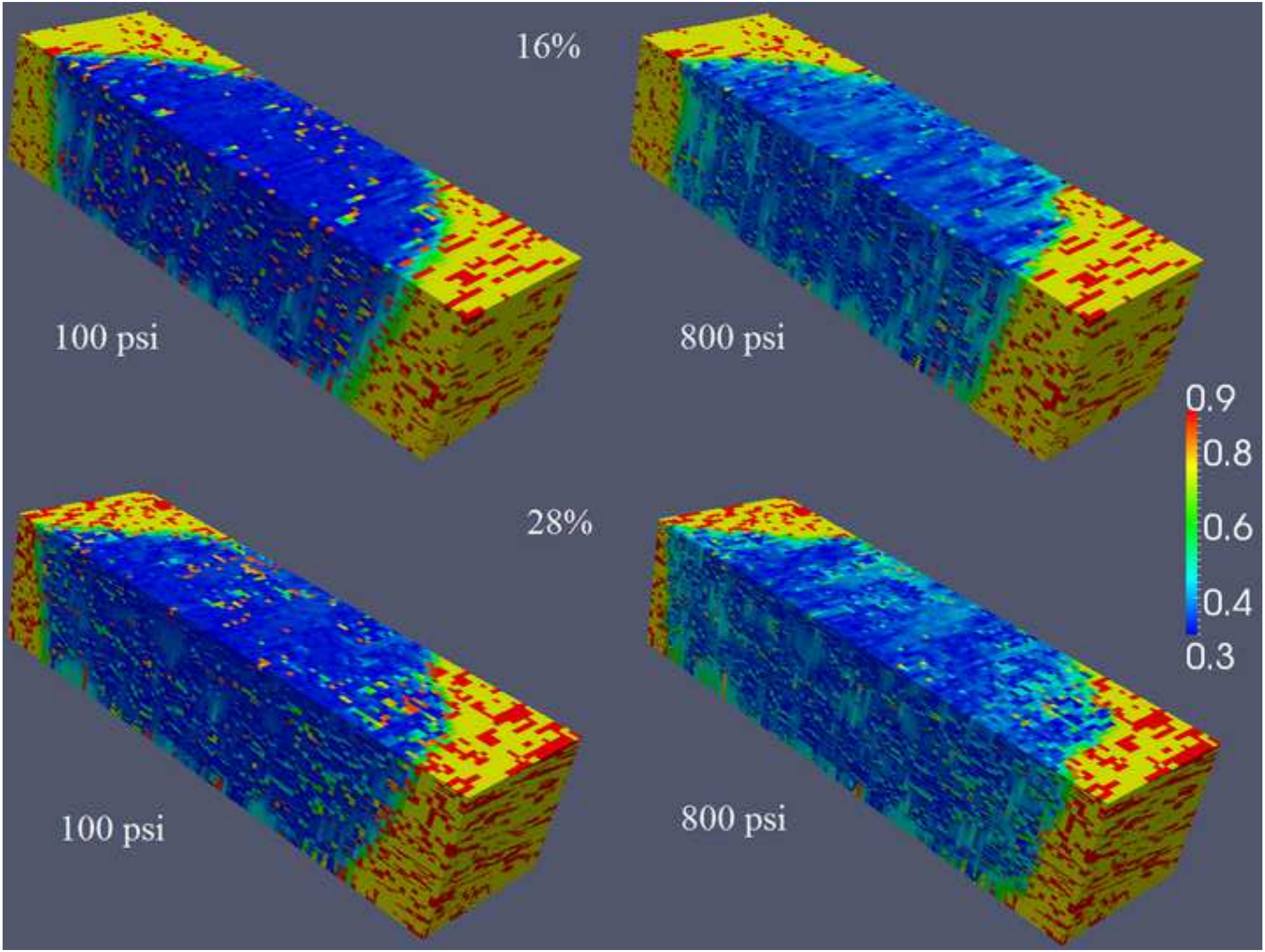

Figure 16
Click here to download Figure: Figure 16.tif

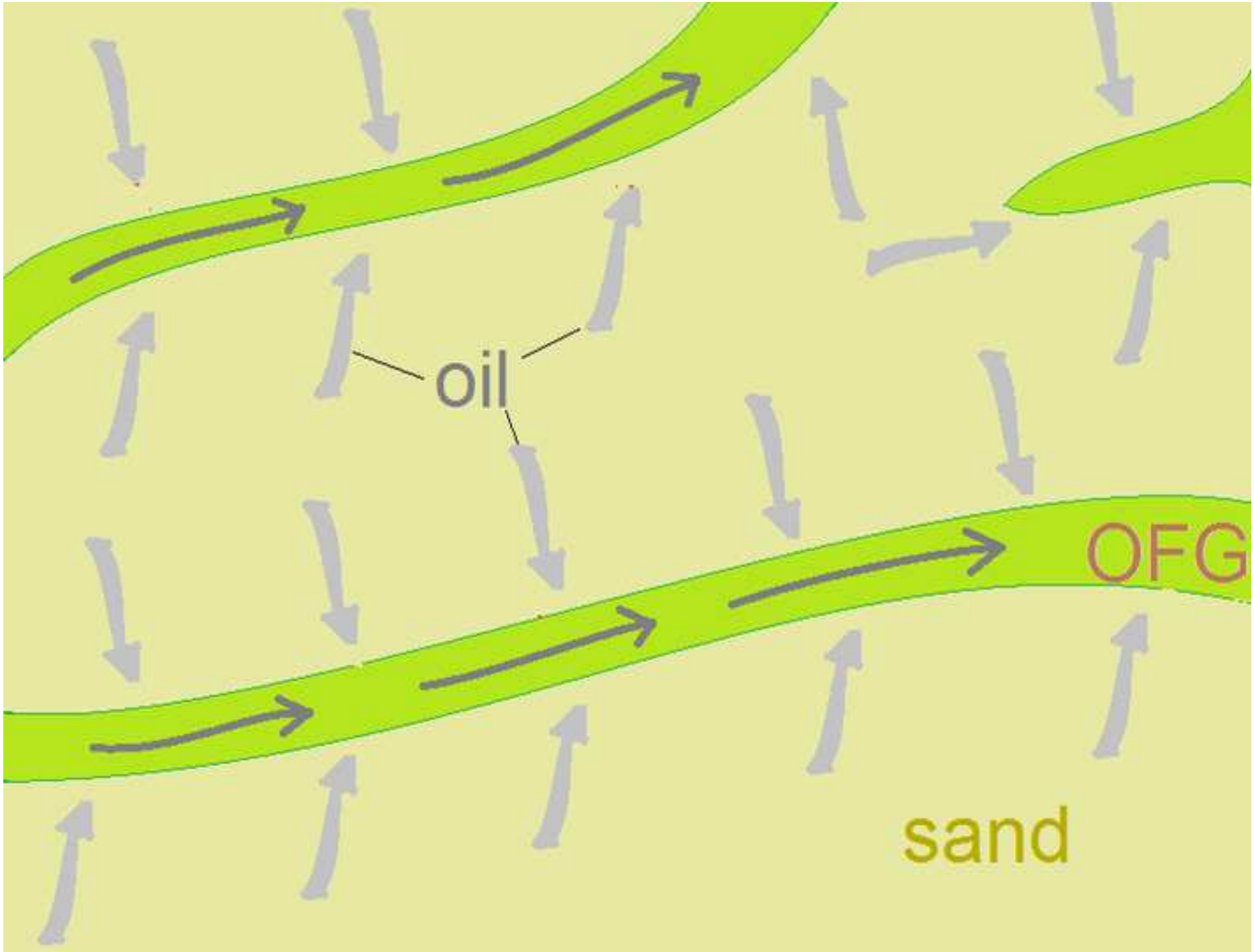

Figure 17
Click here to download Figure: Figure 17.tif

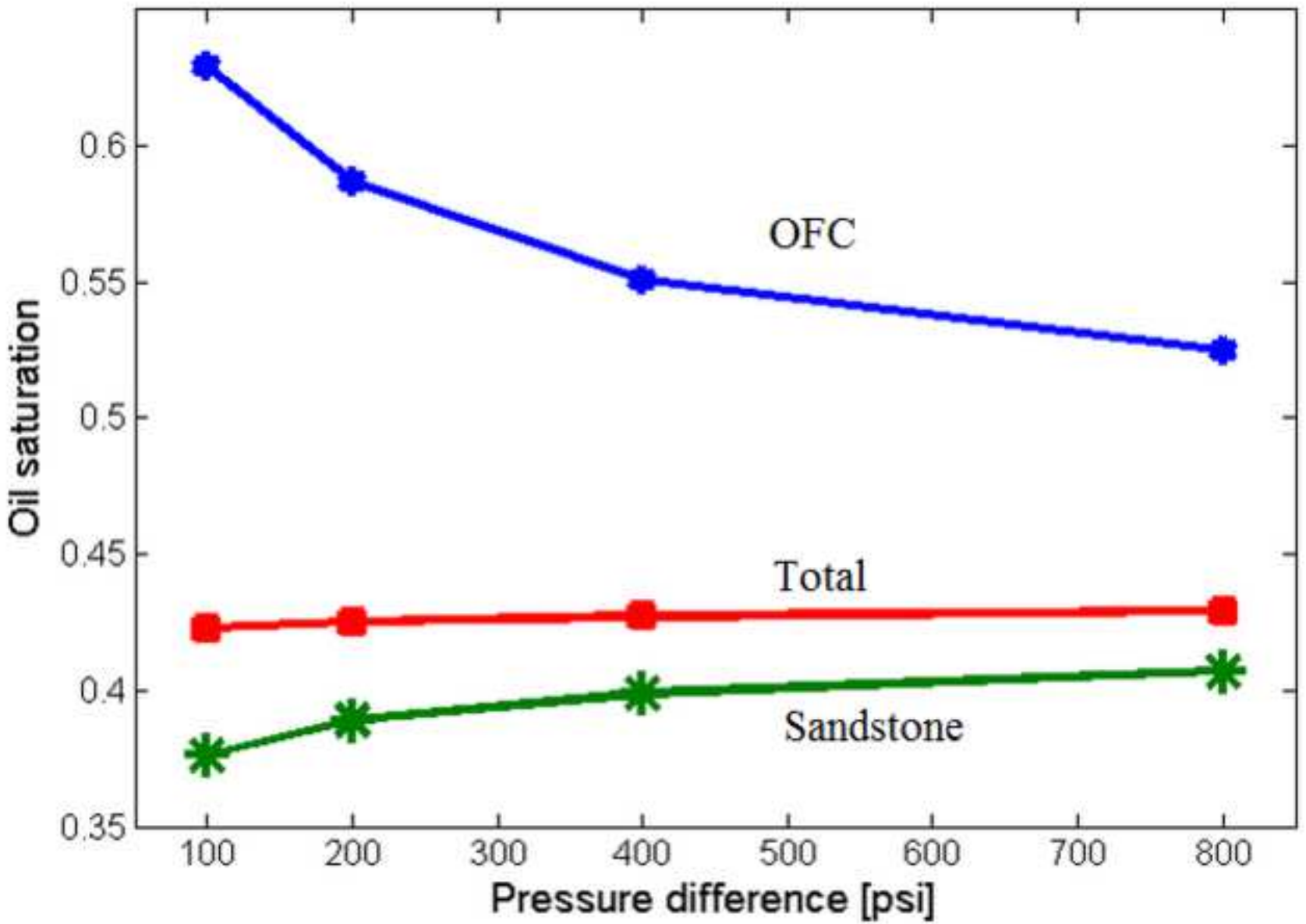

Figure 18
Click here to download Figure: Figure 18.tif

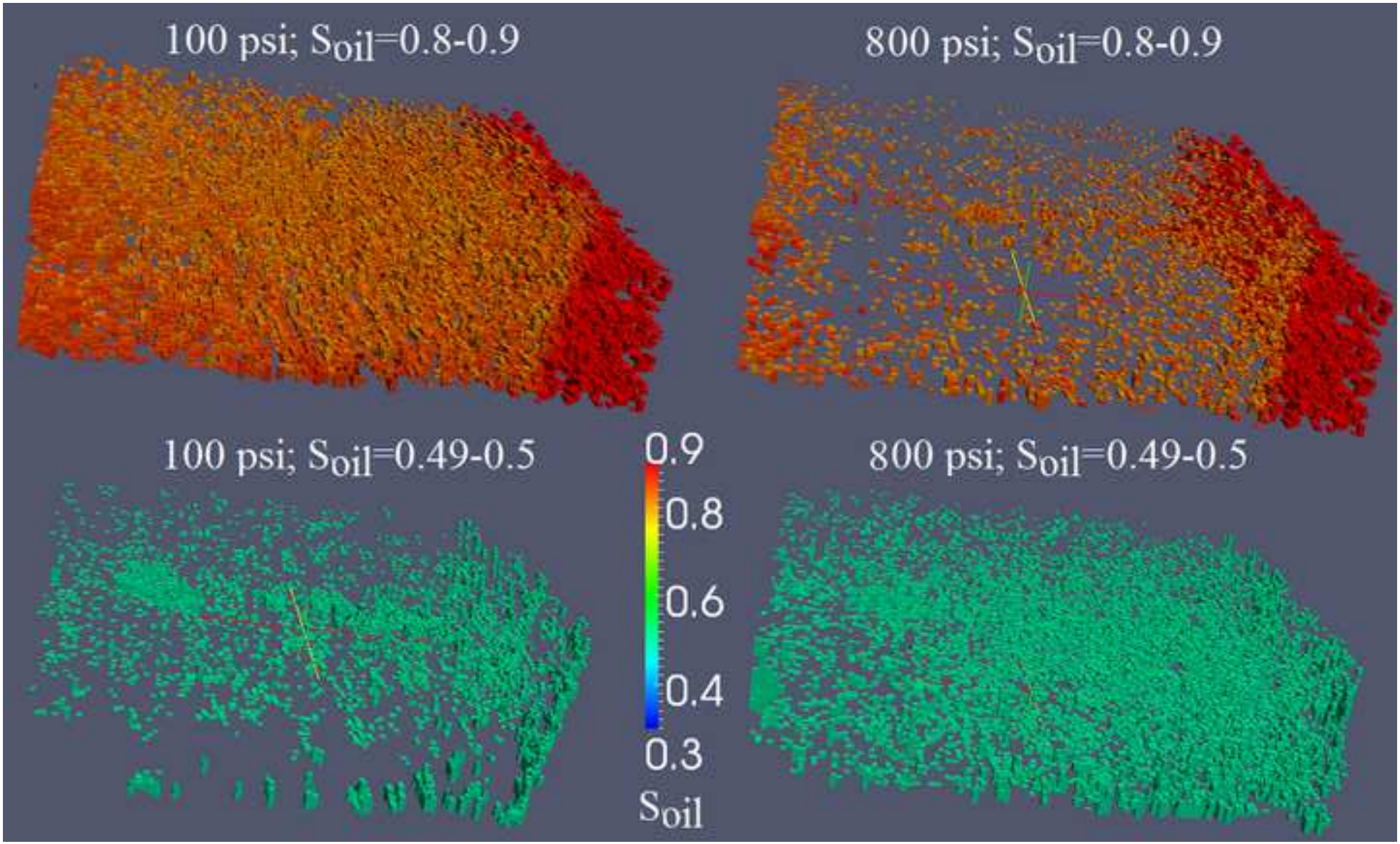

Figure 19
Click here to download Figure: Figure 19.tif

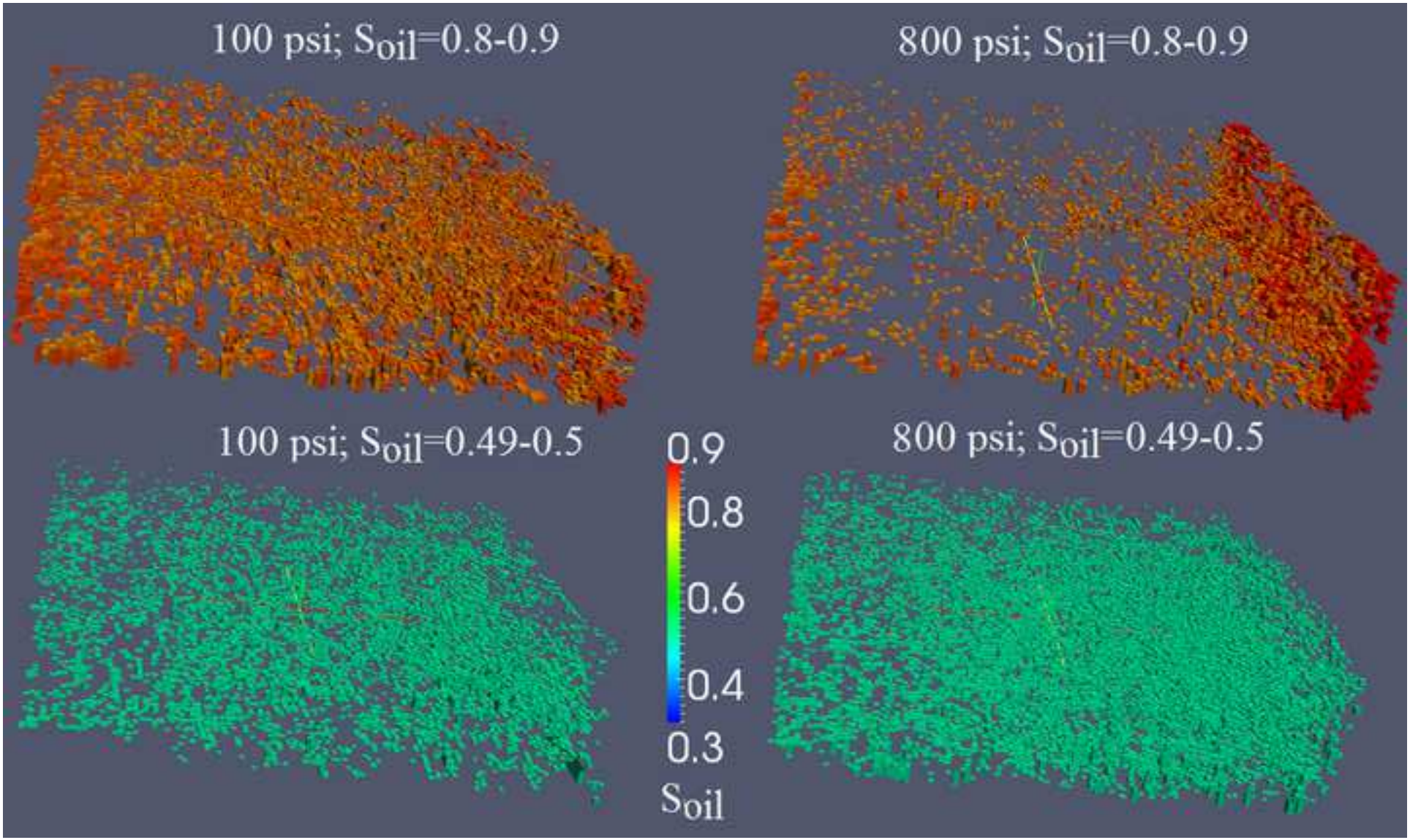

Table 1: Hierarchy of Unit Types from largest (IV) to smallest (I) strata types

IV	channel-belt deposit				
III	compound bar deposits[1]				major channel fills
II	unit bar deposits			cross-bar channel fills	concave-up sand
I	open-framework gravel set[2]	gravelly sand set	sand set	concave-up sand	concave-up sand

[1.] typical dimensions (largest unit type): *750 x 500 x 2 m^3*

[2.] typical dimensions (smallest type): decimeters to meters long and wide, centimeters to decimeters thick (Lunt et al., 2004a,b).

Table 2: Parameters of six realizations: proportion of OFG material (column 2), geometric mean permeability (column 3), proportion of connected OFG cells among OFG cells (column 4), presence/absence of spanning clusters in realization (column 5) mean size of OFG and sand clusters in x, y and z directions (last three columns).

Realization #	OFC Proportion (%)	Geometric Mean Permeability (mD)	Proportion of Connected OFC Cells Among OFC Cells (%)	Do Clusters Span Opposing Boundaries?	Mean size OFC/sandstone clusters, *x* direction	Mean size OFC/sandstone clusters, *y* direction	Mean size OFC/sandstone clusters, *z* direction
1	28	226	91	yes	1.6/4.0	2.8/6.7	3.1/7.5
2	26	205	85	yes	1.5/4.3	2.8/7.3	3.0/8.0
3	24	193	71	yes	1.5/4.4	2.5/7.4	2.8/8.2
4	22	174	53	yes	1.4/4.8	2.6/8.5	2.8/9.1
5	19	149	6.8	no	1.3/5.6	2.2/8.9	2.6/10.5
6	16	136	0.9	no	1.3/6.1	2.3/10.7	2.4/11.3

Table 3. Total oil production normalized by movable pore volume. The pressure difference between wells is 200 psi. We quantify sweep efficiency (*SE*) as the percentage of oil removed from a reservoir before water breakthrough: $SE = 1 - S_{break}$, where S_{break} is the resulting (after water breakthrough) oil saturation normalized by the initial moveable oil volume S_{init}. The ratio between sweep efficiency when the pressure gradient is in the *x* direction and when it is in the *y* direction presented in a fourth column.

Realization	Up to water breakthrough (*y* direction)	Up to water breakthrough (*x* direction)	Sweep efficiency ratio between x and y directions (%)	Up to injection of one movable pore volume water (*y* direction)	Up to injection of one movable pore volume water (*x* direction)
1	0.279	0.379	16.1	0.418	0.545
2	0.263	0.378	18.4	0.434	0.516
3	0.257	0.384	20.6	0.427	0.538
4	0.235	0.398	27.1	0.349	0.467
5	0.245	0.371	20.0	0.341	0.419
6	0.254	0.366	17.5	0.279	0.483